



HAL
open science

Improved Near-Surface Continental Climate in IPSL-CM6A-LR by Combined Evolutions of Atmospheric and Land Surface Physics

Frédérique Cheruy, Agnès Ducharne, Frédéric Hourdin, Ionela Musat, Étienne Vignon, Guillaume Gastineau, Vladislav Bastrikov, Nicolas Vuichard, Binta Diallo, Jean-Louis Dufresne, et al.

► **To cite this version:**

Frédérique Cheruy, Agnès Ducharne, Frédéric Hourdin, Ionela Musat, Étienne Vignon, et al.. Improved Near-Surface Continental Climate in IPSL-CM6A-LR by Combined Evolutions of Atmospheric and Land Surface Physics. *Journal of Advances in Modeling Earth Systems*, 2020, 12 (10), pp.e2019MS002005. 10.1029/2019ms002005 . hal-03013156

HAL Id: hal-03013156

<https://hal.science/hal-03013156v1>

Submitted on 18 Nov 2020

HAL is a multi-disciplinary open access archive for the deposit and dissemination of scientific research documents, whether they are published or not. The documents may come from teaching and research institutions in France or abroad, or from public or private research centers.

L'archive ouverte pluridisciplinaire **HAL**, est destinée au dépôt et à la diffusion de documents scientifiques de niveau recherche, publiés ou non, émanant des établissements d'enseignement et de recherche français ou étrangers, des laboratoires publics ou privés.

RESEARCH ARTICLE

10.1029/2019MS002005

Special Section:

The IPSL Climate Model Used in CMIP6**

Key Points:

- The representation of the land-atmosphere coupled system by the IPSL model is thoroughly evaluated
- Improvements with respect to previous versions are documented in the context of the Coupled Model Intercomparison Project, CMIP
- Advanced parameterization of land and atmospheric processes, tuning of the radiation, and the turbulent mixing yielded many improvements

Supporting Information:

- Supporting Information S1

Correspondence to:

F. Cheruy,
frederique.cheruy@lmd.jussieu.fr

Citation:

Cheruy, F., Ducharne, A., Hourdin, F., Musat, I., Vignon, É., Gastineau, G., et al. (2020). Improved near-surface continental climate in IPSL-CM6A-LR by combined evolutions of atmospheric and land surface physics. *Journal of Advances in Modeling Earth Systems*, 12, e2019MS002005. <https://doi.org/10.1029/2019MS002005>

Received 30 DEC 2019

















Accepted 17 JUL 2020

Accepted article online 30 JUL 2020

©2020. The Authors.

This is an open access article under the terms of the Creative Commons Attribution License, which permits use, distribution and reproduction in any medium, provided the original work is properly cited.

Improved Near-Surface Continental Climate in IPSL-CM6A-LR by Combined Evolutions of Atmospheric and Land Surface Physics

Frédérique Cheruy¹ , Agnès Ducharne² , Frédéric Hourdin¹ , Ionela Musat¹ , Étienne Vignon³ , Guillaume Gastineau⁴ , Vladislav Bastrikov⁵ , Nicolas Vuichard⁵ , Binta Diallo¹ , Jean-Louis Dufresne¹ , Josefine Ghattas⁶ , Jean-Yves Grandpeix¹, Abderrahmane Idelkadi¹, Lidia Mellul¹, Fabienne Maignan⁵ , Martin Ménégoz⁷, Catherine Ottlé⁵ , Philippe Peylin⁵ , Jérôme Servonnat⁵ , Fuxing Wang¹ , and Yanfeng Zhao¹

¹Laboratoire de Météorologie Dynamique (LMD)/IPSL/Sorbonne Université/CNRS, UMR 8539, Paris, France, ²Milieux environnementaux, transferts et interaction dans les hydrosystèmes et les sols (Metis)/Sorbonne Université/IPSL/CNRS/EPHE, Paris, France, ³Environmental Remote Sensing Laboratory (LTE), École Polytechnique Fédérale de Lausanne (EPFL), Lausanne, Switzerland, ⁴Laboratoire d'Océanographie et du Climat: Expérimentation et Approches Numériques (Locean)/Sorbonne Université/IPSL/CNRS, Paris, France, ⁵Laboratoire des Sciences du Climat et de l'Environnement, IPSL, unité mixte CEA-CNRS-UVSQ, Gif sur Yvette, France, ⁶Institut Pierre Simon Laplace (IPSL), CNRS, Paris, France, ⁷Institut des Géosciences de l'Environnement (IGE), Univ. Grenoble Alpes, CNRS, 38000, Grenoble, France

Abstract This work is motivated by the identification of the land-atmosphere interactions as one of the key sources of uncertainty in climate change simulations. It documents new developments in related processes, namely, boundary layer/convection/clouds parameterizations and land surface parameterization in the Earth System Model of the Institut Pierre Simon Laplace (IPSL). Simulations forced by prescribed oceanic conditions are produced with different combinations of atmospheric and land surface parameterizations. They are used to explore the sensitivity to the atmospheric physics and/or soil physics of

- major biases in the near surface variables over continents,
- the energy and moisture coupling established at the soil/atmosphere interface in not too wet (energy limited) and not too dry (moisture limited) soil moisture regions also known as transition or “hot-spot” regions,
- the river runoff at the outlet of major rivers.

The package implemented in the IPSL-Climate Model for the Phase 6 of the Coupled Models Intercomparison Project (CMIP6) allows us to reduce several biases in the surface albedo, the snow cover, and the continental surface air temperature in summer as well as in the temperature profile in the surface layer of the polar regions. The interactions between soil moisture and atmosphere in hotspot regions are in better agreement with the observations. Rainfall is also significantly improved in volume and seasonality in several major river basins leading to an overall improvement in river discharge. However, the lack of consideration of floodplains and human influences in the model, for example, dams and irrigation, impacts the realism of simulated discharge.

Plain Language Summary Land surface-atmosphere interactions play an essential role in the climate system. They strongly modulate the regional climates and have impacts on the global scale for instance through freshwater release into the oceans. Climate hazards (heat waves, droughts) and their impacts on populations also strongly depend on interactions between land and atmosphere and on their evolution with climate change. Climate models are precious tools to investigate how the Earth climate behaves. The sixth phase of the Climate Model Intercomparison Project (CMIP6) provides important tools to measure the progress and address the remaining open questions regarding the continental climate modeling. The representation of the land-atmosphere coupled system by the IPSL-Climate Model involved in CMIP6 is thoroughly evaluated against observations and compared with simulations using the CMIP5 version. Several biases concerning the temperature over land and over the ice sheets and with the snow cover are significantly reduced. Numerous improvements were made developing advanced parameterizations and tuning of the radiation and of the turbulent mixing in the atmospheric model. The realism of the seasonal

cycle of hydrological variables such as the precipitation or the river discharge is also improved over many regions. The new treatment of hydrology paves the way for future developments on water resource aspects in the climate model.

1. Introduction

Earth's climate and its evolution are determined by interactions between the ocean, the atmosphere, ice caps, and land surfaces under the external solar forcing and the atmospheric composition. For these reasons, numerical models need to couple all these components of the system when they are used for running climate projections to anticipate the impacts of climate change. In this general framework, the land surface-atmosphere interactions strongly modulate the regional climate (e.g., Seneviratne et al., 2010); they particularly control climate hazards, and their consequences (Jaeger & Seneviratne, 2011; Miralles et al., 2014) impact the freshwater discharge into the oceans and, in turn, the thermohaline circulation (Peterson et al., 2002). They rely on complex overlap of multiple land-atmosphere feedback processes and depend on the representation of the interactions between the soil moisture and the boundary layer through the partition of the available energy at the surface in sensible and latent heat, the impact on radiation (Betts et al., 1996; Eltahir, 1998; Schär et al., 1999), the representation of the convection and its sensitivity to sub-grid scale heterogeneities (Guilod et al., 2015; Taylor et al., 2011, 2012), the representation of soil moisture, and the possible interplay with the atmospheric circulation (Boé, 2013; Hohenegger & Stevens, 2018). The complexity and the variety of processes involved make the land-atmosphere interactions one of the key sources of uncertainty in climate change simulations at regional scale. As an example, analyses of CMIP5 models revealed considerable spread in the ability of models to reproduce observed correlation between precipitation and soil moisture in the tropics (Williams et al., 2012).

The various phases of the Climate Model Intercomparison Project (CMIP) give important milestones to measure the progress and the remaining open questions concerning the climate modeling and in particular the parameterization of the land surface-atmosphere interactions. Between Phases 5 and 6 of CMIP, significant efforts have been devoted to improving the atmospheric (Hourdin et al., 2020), the land surface, and hydrological components of the Earth System Model of Institut Pierre Simon Laplace (IPSL) and to tuning the Climate Model (CM). When the fully coupled model is used, compensating errors can hide the role played by the sub-grid scale processes that regulate a large part of the exchanges of energy, water, and matter between the surface and the free atmosphere or constrain the related parameterizations to work in unrealistic conditions (e.g., Diallo et al., 2017; Roehrig et al., 2013). On the contrary, working with individual components impedes the activation of important couplings and feedbacks. Configurations with prescribed sea surface temperature (SST) and sea ice concentration (SIC) allow us to overcome these difficulties. These configurations are referred to as Atmospheric Model Intercomparison Project (AMIP) configurations. Together with an intermediate configuration, such as a nudged configuration in which the large-scale dynamics (i.e., the zonal and meridional wind components) is nudged towards reanalysis (Cheruy et al., 2013; Coindreau et al., 2007; Diallo et al., 2017), these AMIP-like configurations are used here to assess how realistic the continental surface-atmosphere interactions simulated by the IPSL-CM are and to help interpret the fully coupled simulations produced with the atmospheric (LMDZ) and land surface (ORCHIDEE) components of the IPSL-CM.

The focus of the present analysis is put on the processes which control the energy and moisture exchange at the surface. Main features of the near surface climate over continents in the historical simulations done with the full IPSL-CM are documented in a companion paper (Boucher et al., 2020), where the biogeochemical aspects of the land surface-atmosphere coupling are considered.

In section 2, the major changes of LMDZ, ORCHIDEE, and their interface are summarized, and the simulations used for the analyses are described. The evolution of the main biases in near-surface variables since CMIP5 is analyzed in the third section, and sensitivity studies are used to identify the source of these biases. The role of the parameterizations and of the adjustment or tuning (Hourdin et al., 2017) is discussed. In the fourth section, the impact of the modified parameterizations on essential variables of the coupling (radiation, evaporation, precipitation, and surface soil moisture) is discussed for hotspot regions (Koster et al., 2004) such as Central North America and a region in the Sahel where the land surface coupling is strong but

largely model-dependent (Boé & Terray, 2008; Hohenegger et al., 2009). The fourth section also deals with river discharge and its response to precipitation. It is a central target for a CM for several reasons: One of them is that the freshwater discharge into the Arctic Ocean from the boreal rivers affects the global climate system by impacting the thermohaline circulation (Peterson et al., 2002). It is also a valuable source of information for utilization of global water resources and prevention of floods and drought which can both increase the risk for populations in the context of climate change (Arnell & Gosling, 2013; Schewe et al., 2014). For some basins, it is possible to compare the results with observations which provides an assessment of the hydrological cycle over major watersheds. In the last section, the results are summarized, and directions for further improvements are presented.

2. Model Physical Content and Setup of the Simulations

2.1. The Atmospheric Model

LMDZ is the atmospheric General Circulation Model (GCM) that has been developed for about 30 years at the Laboratoire de Météorologie Dynamique (LMD). The versions of LMDZ used for Phases 5 and 6 (hereafter called 6A) of CMIP together with the configuration adopted are described in Hourdin et al. (2006) and Hourdin et al. (2020). The main contribution of IPSL to CMIP5 was done with a package hereafter called AP and referred to as “IPSL-CM5A” in the CMIP5 database. Version 6A is an improved version of the “new physics” package, a preliminary version of which has been tested for CMIP5 (Hourdin et al., 2020) and is referred to as “IPSL-CM5B-LR” in the CMIP5 database. The changes from the AP to the “new physics” version are linked to a complete rethinking of the parameterizations of turbulence, convection, and clouds and are described in Hourdin et al. (2013). The main model modifications between the “new physics” and 6A are the revision of the eddy diffusion Yamada (1983) 1.5 order turbulent scheme already implemented in the new physics, the introduction of a stochastic triggering designed to make the frequency of occurrence of new convective systems within a mesh aware of the grid cell size (Rochetin, Couvreur, et al., 2014; Rochetin, Grandpeix, et al., 2014), a modification of the thermal plume model for the representation of stratocumulus clouds (Hourdin et al., 2019), the introduction of the latent heat release associated with water freezing (not accounted for so far), and a new parameterization of non orographic gravity waves targeting the representation of the quasi-biennial oscillation (QBO). These changes were accompanied by a significant refinement of the vertical grid, both for the QBO issue and for a better representation of boundary layer clouds. The radiative codes in LMDZ are inherited from the ECMWF weather forecast model. In version AP a “wide band” spectral model was used both in the thermal infrared and in the shortwave (SW) spectrum (Morcrette, 1991). In version 6A, the infrared part was replaced by the RRTM code (Mlawer et al., 1997), based on a k-correlated scheme with 16 spectral bands. For the SW radiation the number of spectral intervals increased from 2 to 6 in order to better distinguish near infrared, visible, and ultraviolet radiation.

For the setting of the 6A version, particular attention was paid to the very stable boundary layers that occur over the ice sheet plateaus, sea ice, and boreal lands. Such boundary layers can experience very weak and intermittent turbulence even close to the ground surface, pushing the current state-of-the-art subgrid mixing parameterizations and underlying physical assumptions to their limits and even beyond. Together with the refinement of the vertical grid, the computation of the eddy diffusion in the Yamada (1983) scheme was revised. Minimum threshold values of the mixing length and of the stability functions of the eddy diffusion coefficient have been significantly decreased (Table 2) to allow for a cutoff of turbulence at a few meters above the surface in the very stable conditions encountered over the Antarctic Plateau and to obtain more realistic sharp vertical gradients in very stable atmospheric boundary layers (ABLs) (Vignon et al., 2017). Such threshold values are often set in operational numerical models to compensate for the nonrepresentation of subgrid mixing processes and to prevent excessive near-surface cooling over land in winter (e.g., Sandu et al., 2013). The sensitivity of the continental temperature at seasonal and diurnal scale to the values of the thresholds will be discussed in sections 3.2 and 3.4. Moreover, a new numerical treatment of the Turbulent Kinetic Energy (TKE) equation in the new scheme prevents an artificial cutoff of the turbulence at standard time step values that could occur in previous model versions even at moderate stability (Hourdin et al., 2020; Vignon, 2017).

The need to remove thresholds in the turbulence scheme to properly model the stable ABL over the Antarctic Plateau also raises the need to parameterize more explicitly the additional sources of mixing in

other regions of the globe such as orography-induced small scales gravity-wave drag (Steenefeld et al., 2008) or the drag induced by vertical obstacles penetrating the boundary layers such as trees (Masson & Seity, 2009; Nepf, 1999). Due to the refinement of the vertical grid of the model several layers can intersect high vegetation. The loss of large-scale kinetic energy due to these drags is converted into TKE. The evaluation of the orography-induced gravity-wave drag is based on the scheme developed by Lott (1999), while the drag due to high vegetation is set proportional to the vegetation fraction, which penetrates the boundary layer. The two subgrid scale mixing processes generate TKE, which is accounted for in the prognostic equation (see Appendix A for details). The impact of these new developments on near-surface atmospheric variables are illustrated in section 3.4.

2.2. The Land Surface Model

The land surface is described by the ORCHIDEE model v2.0. The ORCHIDEE model v2.0 computes primarily the fluxes of energy, water, and carbon that are exchanged between the different soil and plant reservoirs and the exchange of these fluxes with the atmosphere. In addition, it computes the stocks of water and carbon in the different soil and plant reservoirs and the energy stored in the different soil and snow layers. Model state variables are prognostic, including the Leaf Area Index (LAI), as they are updated at each time step after the calculation of the fluxes between all reservoirs. The module computing dynamically the LAI, the vegetation albedo, and the soil water stress function applied to transpiration is activated for all CMIP experiments, except for the HighResMIP one (see section 2.4) that uses prescribed values. The vegetation properties are defined by plant functional types (PFTs), and their fraction within each grid cell is globally set from land cover maps that were derived specifically for the CMIP6 simulations (Lurton et al., 2020). These maps combine the historical maps from the land use harmonization database (LUH2v2h, Hurtt et al., 2011) and the maps derived from satellite observations (Bontemps et al., 2015). See <https://orchidas.lscce.ipsl.fr/dev/lccci/>, for more information. The water and energy budgets are computed at the same time-step as the atmospheric physics (Hourdin et al., 2020) using classical soil-vegetation-atmosphere transfer (SVAT) parameterizations. The most relevant modification since the version used for CMIP5 is related to the soil hydrology, the snow scheme, and the background albedo. The 2-layer conceptual parameterization (hereafter referred to as “Choi”, (Ducoudré et al., 1993) used for CMIP5 is a double bucket model that has an upper layer with a varying depth that can appear at the surface after a rainfall event to deal with short-time processes and disappears after dry spells (Manabe, 1969). “Choi” refers to the scheme that Choissnel developed and tested for cultivated area over France. Laval (1988) showed that this model improved the sensible and latent heat flux computation on the original bucket model when introduced into the LMD Atmospheric GCM. In the version used for CMIP6, the vertical water transport is described using Richard’s equation (De Rosnay et al., 2002; d’Orgeval et al., 2008) discretized with 11 layers. The layer thickness increases downwards and is doubled between each consecutive layer. The soil moisture column is active over 2 m; a free drainage condition is imposed at the bottom of the reservoir. This scheme hereafter called ctrl, as it is now the reference version for IPSL-CM, is sometimes referred to as the “11-layer” ORCHIDEE scheme. The potential of improvement of an early version of this scheme coupled with the AP and “new physics” versions of LMDZ has been tested in Cheruy et al. (2013) and Campoy et al. (2013). The soil thermodynamics and in particular the soil thermal properties have been revised by Wang et al. (2016). They have a significant impact on the surface temperature and its high frequency variability in all regions except for the moist regions (Cheruy et al., 2017). The vertical discretization for temperature is now identical to that adopted for water, with a minimum soil depth increased to 10 m (and even 90 m when the soil freezing is accounted for) so that the condition of zero flux at the bottom can be checked globally and annually. The soil properties (hydraulic and thermal) depend on soil moisture and soil texture, with three possible classes (sandy loam, loam, and clay loam). The dominant soil texture is assigned to each grid cell, based on the 1° soil texture map of Zobler (1986). The soil heat capacity is parameterized as a function of the heat capacity of the dry soil and the liquid water profile and when necessary the ice profile. The soil freezing is allowed and diagnosed in each soil layer following a scheme proposed by Gouttevin et al. (2012), but the latent heat release/consumption associated with water freezing/thawing is not accounted for. The freezing state of the soil mainly impacts the computation of soil thermal and hydraulic properties, reducing for instance the water infiltration capacity at soil surface. Wang et al. (2013) replaced the snow scheme of Chalita and Le Treut (1994) by a three-layer scheme of intermediate complexity largely inspired by that proposed by Boone and Etchevers (2001). A routing module (Guimberteau et al., 2012; Polcher, 2003) transforms the

total runoff in each subbasin into river discharge through the ocean. This routing scheme relies on a cascade of linear reservoirs along the river network (stream reservoirs), complemented in each grid cell by two local reservoirs, to account for the delay between surface runoff and drainage, on the one hand, and overland and groundwater flow to the stream reservoir, on the other hand. When using Choi, which does not separate total runoff into surface runoff and drainage, an arbitrary partitioning is imposed, with 5% feeding the fast reservoir and 95% feeding the slow reservoir (Guimberteau et al., 2014). In the multilayer version of ORCHIDEE, evaporation from bare soil following a supply and demand pattern that is controlled by the moisture present in the surface layers of the soil (the four soil layers of the model closest to the surface), which evaporates at the potential rate if the soil moisture supply meets the demand.

The continental ice-covered surfaces (ice sheets and glaciers) are not included in ORCHIDEE, but they are treated in a specific module within LMDZ. Momentum and heat roughness heights as well as visible and near infrared albedos are set to constant values representative of snow conditions over the Antarctic Plateau (Vignon et al., 2018). The heat transfer in the snow and ice is parameterized as a conductive process with a fixed thermal inertia (Hourdin, 1992). The vertical grid is made of 11 vertical levels to represent the e-folding damping of thermal waves with typical periods from 1,800 seconds to 240 years. The value of the snow thermal inertia was calibrated to obtain realistic surface temperature and diurnal cycle amplitudes in Antarctica (Vignon et al., 2017).

Le Quéré et al. (2018) have recently used a version of ORCHIDEE (referred to as Orchidee-Trunk), which is similar to the version used for CMIP6 in an intercomparison project focussing on the carbon and water fluxes where 15 other land surface models (LSMs) were involved. The skill scores obtained by ORCHIDEE are among the highest for most of the variables considered in this study and in particular for evapotranspiration, LAI, and runoff (see table B2 in Le Quéré et al., 2018), which are directly involved in our study.

2.3. The Coupling with the Surface

In the surface layer the boundary layer model uses Monin-Obukhov theory and bulk formulations proposed by Louis et al. (1982) to parameterize turbulent fluxes. Several modifications were made in the representation of the surface layer of LMDZ as well. First, and consistently with the changes done in the boundary layer to allow strong decoupling in stable atmospheres, the so-called “long-tail” stability functions from Louis et al. (1982) that artificially enhance the surface turbulent fluxes in stable conditions were replaced by more realistic “short-tail” functions from King et al. (2001). This was shown to significantly improve the representation of surface temperature on the very flat ice sheet of the Antarctic plateau.

A second important change is related to the computation of surface roughness height z_0 . At the surface itself, heat and humidity transfer are dominated by molecular diffusion, which is less efficient than the momentum transfer due to the pressure forces that are related to the geometry of the roughness elements of the surface (Garratt & Hicks, 1973). For these reasons the roughness heights for the momentum are currently much higher than that of heat or humidity. While a unique value was used in former versions for all the model state variables, a different value is now used for horizontal momentum $z_{0,m}$ and thermodynamical variables $z_{0,h}$ or tracers $z_{0,t}$ for all individual type of subsurface (land, sea, sea-ice, continental-ice). For each PFT ORCHIDEE used a prescribed value for the roughness height for heat and moisture independent of the development of the vegetation over continents. For a grid point composed of different types of vegetation, an effective surface roughness is calculated based on the flux conservation over the grid point. This value was also used for $z_{0,m}$ in LMDZ. Measurement campaigns often suggest that the roughness height for heat should be one-tenth of that for momentum for homogeneous surfaces and even less for heterogeneous surfaces (Malhi, 1996). Some studies propose that over vegetated areas the roughness height can be parameterized as a function of the LAI. This is the case for the model proposed by Massman (1999) and tested by Su et al. (2001), which has been implemented in ORCHIDEE v2.0. In forced mode, the dynamic roughness heights computed for each PFT as a function of the LAI help reduce latent heat calculated in winter on temperate sites, in good agreement with multiannual Fluxnet measurements (Figure S1, (<https://fluxnet.fluxdata.org/data/la-thuille-dataset/>)). Still in forced mode, the dynamic roughness heights impact the river discharge at the scale of individual watersheds with significant improvements for the Danube and the Mississippi watersheds (not shown). The impact of activating the dynamical roughness height in coupled simulations is limited for the considered space and time scales (see section 3.4), but the option is activated for all CMIP6 simulations.

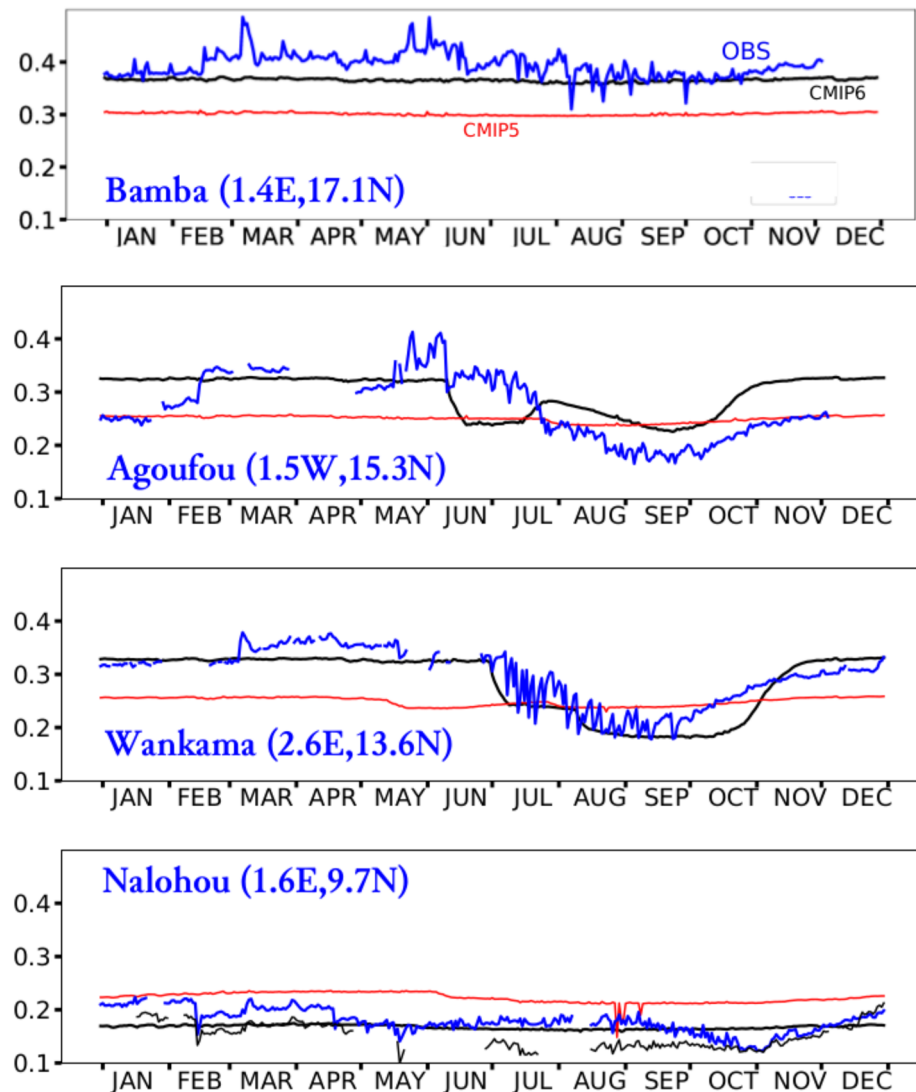


Figure 1. Time series of the surface albedo for year 2006 at Bamba, Agoufou, Wankama, and Nalohou stations, from top to bottom panel, respectively. Local observations (blue) are compared with nudged simulations for CMIP5 (red) and CMIP6 (black) physics. The simulation is forced to follow the synoptic variability by relaxing the large scale circulation toward meteorological analyses, which allows direct comparison of the time series; observations were obtained in 2006, the year of the AMMA Special Observing Period, and are available from the AMMA-CATCH database (<http://www.amma-catch.org>).

Another important change in ORCHIDEE is related to the individual albedo of the bare soil and of the 14 vegetated PFT, which is now optimized with respect to MODIS observations. This calculation of the individual albedo leads to significant improvements, especially over deserts and semiarid areas where the albedo was significantly underestimated. The improvement is illustrated by a comparison of the time series of the albedo simulated with the CMIP5 and the CMIP6 versions of the model and measured at the sites in the Sahel (Figure 1). The simulation is forced to follow the synoptic variability by relaxing the large-scale circulation toward meteorological analyses, which allows direct comparison of the time series of the observations and the simulations (Cheruy et al., 2013; Coindreau et al., 2007).

The near-surface (i.e., 2 m) temperature (CMIP6 variable *tas*, which is one of the most analyzed variables in CMs especially in relation to climate change impacts) is diagnosed through a procedure based on the Monin-Obukhov theory (Hess, 1995). The procedure involves both surface and first model-level variables. In situations when turbulence is very weak and the atmospheric layer above the surface is dry but the

Table 1

Reference Simulations: APChoi Corresponds to the IPSL-CM5A Configuration Used for CMIP5, and 6Actrl Corresponds to the IPSL-CM6A Configuration Used for CMIP6

Experiment	Boundary conditions	Atmosphere	Vertical levels	Land surface	duration
APChoi	Clim	AP	39	Choi	20 years
APctrl	Clim	AP	39	Ctrl	20 years
6Achoi	Clim	6A	79	Choi	20 years
6Actrl	Clim	6A	79	Ctrl	20 years
AMIP	Actual	6A	79	Ctrl	1978–1998

Note. The boundary conditions used (climatology [clim] or actual values of SST and Sea-Ice [actual]) are indicated in the second column.

surface soil moisture is far from the residual moisture, the procedure occasionally fails, leading to nonphysical values for one timestep. When the procedure fails screen level temperature can reach 450 K and screen level specific humidity becomes negative (see Appendix B). Since the problem occurs rarely, and when it does occur it is only during one timestep in the day (very exceptionally it can occur during two or more timesteps in the day), it was undetected in the final version used for the production of the CMIP6. The problem affects the maximum daily near-surface temperature, the minimum daily near-surface relative humidity, and marginally the daily averages of these quantities. It occurs approximately 1,700 times (respectively, 2,200 times) in a simulated year of the AMIP (respectively, PreIndustrial Control [piControl], Eyring et al., 2016) experiments, which is very rare compared to the $(365 \times 144 \times 142 \times 96)$ times that the calculation is performed in one year of simulation. The CMIP6 experiments presented in this paper have not been rerun due to the time constraint imposed by the CMIP exercise; however, an a posteriori correction method has been developed. All the CMIP6 data that have been affected by this problem have been either unpublished or corrected a posteriori and republished.

The a posteriori correction method applied to the published data is given in Appendix B with an estimation of the associated uncertainties, which is of the order of several tenths of degrees for the daily values. Due to the low value of the reconstruction errors for the monthly mean values (30 times less than the reconstruction errors of the daily values), it was decided not to make a correction to the monthly values. The great advantage is that the monthly tas values are absolutely consistent across all CMIP6 experiments, regardless of whether the daily values have been corrected or not. According to these investigations we are confident that all the published values can be used safely for climate analysis.

2.4. Setup of the Simulations

To document the impact of the changes described in the previous sections, simulations forced by observed SST and SIC are produced by combining final versions of atmospheric physics (AP and 6A) and of the soil hydrology (Choi and ctrl), namely, APChoi (corresponding to the IPSL-CM5A in the CMIP5 database), APctrl, 6Achoi, and 6Actrl (corresponding to the IPSL-CM6A in the CMIP6 database) (Table 1). A monthly mean climatology of SST and SIC calculated over the years 1978–2008 is used for the simulations in order to minimize the impact of the interannual variability in the evaluation. The 6Actrl experiment is also compared with the results of the AMIP experiment for which a 20-member ensemble has been produced and is published in the CMIP6 database. The impact of the new developments is documented thanks to an additional set of sensitivity experiments with the 6A physics, where the new features of the LSM and the ABL are individually tested (Table 2). The horizontal

Table 2

Sensitivity Experiments for Processes Impacting the Interactions Between the Land Surface and the Atmosphere

AMIP-experiment	Description
NoOro	Deactivating orography induced small scale gravity wave drag
NoTree	Deactivating vertical obstacle penetrating boundary layer drag
NoSnowFreez	Deactivating soil freezing and replacing the snow scheme of Chalita and Le Treut (1994) by Wang et al. (2013)
Noz0Su	Deactivating dynamical roughness heights (Su et al., 2001) and using prescribed values with $z_{0m} = z_{0h}$
6Arsol	Activating resistance to bare soil evaporation
6Aric	No increased mixing in the stable PBL: ric = 0.20 (reference = 0.18) and lmximin = 0
6Aric83lmx	Artificially increased mixing in the stable PBL: ric = 0.143, lmximin = 1m (reference = 0m)
6A-L+	Increased lift effect (SSO): $gk_{lift} = 1.0$
6A-L-	Decreased lift effect (SSO): $gk_{lift} = 0.0$
6A-D+	Increased block flow drag amplitude by (SSO): $gk_{drag} = 1.2$
6A-D-	Decreased block flow drag amplitude by (SSO): $gk_{drag} = 0.2$

Note. The reference atmospheric physics is 6A with 79 vertical levels, and the reference LSM is ctrl. The last four lines of the table refer to the sensitivity experiments to the subgrid scale orography (SSO) schemes; the reference values for 6A are $gk_{lift} = 0.1$ and $gk_{drag} = 0.6$, gk_{lift} (respectively, gk_{drag}) correspond to C_d (respectively, C_l) in Lott (1999).

Table 3
Global Gridded Data Sets Used as Reference

Variable (monthly means)	Data set	Date	Reference
Radiation	CERES-EBAF-L3B-Ed2-8	2001–2012	Kato et al. (2013)
Precipitation	GPCP long-term-mean	1979–2005	Adler et al. (2003)
Evapotranspiration	In situ upscaled products (over land)	1982–2011	Jung et al. (2011)
Evapotranspiration	GLEAM	2001–2011	Martens et al. (2017)
Surface soil moisture	ESA-CCI	2001–2011	Dorigo et al. (2017)
Surface soil moisture	GLEAM	2001–2011	Martens et al. (2017)
Air temperature (min/max daily)	CRU	2001–2010	Harris et al. (2014)
Air temperature	ERA-I	1979–2014	Dee et al. (2011)
Horizontal winds	ERA-I	1979–2014	Dee et al. (2011)
Total precipitable Water	NVAP-M	1988–2009	Vonder Haar et al. (2012)
River discharge	GRDC	1981–2010	Milliman and Farnsworth (2011)
Snow cover	NOAA-CDR-SCE	2000–2009	Robinson et al. (2012)

grid is identical to the published CMIP6-LR data LR stands for Low Resolution and corresponds to approx. $2.5^\circ \times 1.25^\circ$, namely, 144×142 grid points (Hourdin et al., 2020). We also document simulations performed with a much finer grid of 50 km for the HighResMIP part of the CMIP6 exercise (Haarsma et al., 2016). Comparison of these low and high resolution versions allows us to distinguish the part of the model bias linked to the coarse resolution from that more fundamentally related to the model physical content. Nudged simulations in which the large-scale wind fields (zonal and meridional wind components) are relaxed towards the ERA-Interim reanalyzed winds (ERA-I, Table 3) with a time constant of 3 hours are also used and help assess a possible contribution from large-scale circulation deficiencies to the continental bias. Based on previous experience, it is known that a time constant of several hours (3–12) is short enough to constrain the large scale circulation and long enough for the physical parameterizations to fully operate (for wind nudging at least). More details on this approach can be found in Diallo et al. (2017). The first 3 years of all experiments, corresponding to the spin-up time of the hydrological model, are disregarded in the analysis.

2.5. Reference Data Sets

The sets of global gridded data used as a reference to evaluate the sensitivity experiments are listed in Table 3. They consist of a site-observations upscaled products for evaporation (Jung et al., 2011), satellite-based land evaporation, and surface soil moisture derived through data assimilation processes in the Global Land Evaporation Amsterdam Model (GLEAM) (Martens et al., 2017) and the ESA-CCI blended active and passive microwave retrieval of surface soil moisture (Dorigo et al., 2017), CERES-EBAF for surface SW radiation (Kato et al., 2013), and the Global Precipitation Climatology Project (GPCP) monthly product resulting from an integration of various satellite data sets and a gauge measurements analysis over land (Adler et al., 2003) for the precipitation. The total column integrated water vapor is evaluated using the reanalysis and extension of the NASA Water Vapor Project (NVAP) data set which comprises a combination of radiosonde observations, Television and Infrared Operational Satellite (TIROS) Operational Vertical Sounders (TOVS), and Special Sensor Microwave/Imager (SSM/I) data sets (Vonder Haar et al., 2012). The river discharges are extracted from the Global Runoff Data Center (GRDC) database (Milliman & Farnsworth, 2011). The Snow Cover Extent (SCE) is extracted from the output from the Interactive Multisensor Snow and Ice Mapping System (IMS) at the National Ice Center (NIC) processed at Rutgers University and included in the NOAA Climate Data Record (CDR) of Northern Hemisphere (NH) Snow Cover Extent. For the minimum and maximum daily temperature, we used the Climatic Research Unit (CRU) Time-Series (TS) version 4.01 of high-resolution gridded data (Harris et al., 2014).

The observations cover a period of at least 10 years compatible with the SST and SIC climatology used to force the model. We suggest that not considering the exact same periods for the simulations and the

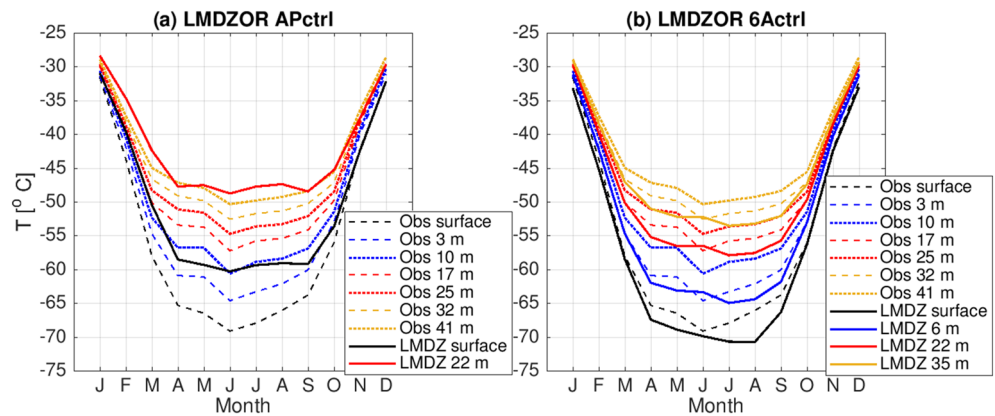


Figure 2. Time series of the near-surface monthly mean temperature at Dome C (75.1S,123.3E), Antarctic Plateau. Solid lines show the APctrl simulation (a) and the 6Actrl simulation (b). Dashed and dotted lines refer to the 2011–2018 observational data set along a 45-m meteorological mast (Genthon et al., 2013).

observations only has a minor impact on the results given that the model internal variability is damped due to the use of a climatological SST and SIC.

In the supplementary material, ERA-5 data (<https://cds.climate.copernicus.eu/cdsapp#!/home>) are used as a benchmark in addition to ERA-Interim data to evaluate the bias in the air-temperature (supporting information Figure S2).

3. Surface Energy Budget and Temperature

3.1. Impact of the Revision of the Eddy Diffusion Parameterization

The improvements resulting from the revision of the turbulent scheme between the AP version and the 6A version of LMDZ are illustrated in Figure 2, showing the mean seasonal cycle of the air temperature for the first three atmospheric levels of LMDZ (version AP and 6A) together with the measurements recorded at six levels on the 45 m height mast at Dome C (75.1S,123.3E), Antarctic Plateau. For version AP (Figure 2a) an overall winter-time warm bias (up to 10 K) in the surface layer is noticeable. This version was also unable to properly reproduce the dynamical behavior of the very stable Antarctic boundary layers (Vignon et al., 2018), and further analysis of the vertical temperature profile in the first few hundred meters above Dome C revealed a significant underestimation of the climatological temperature inversion (not shown). For version 6A, both the near-surface temperature and its vertical gradient are in good agreement with observations from the surface up to the top of the mast (Figure 2). The dynamics of very stable boundary layers is also much better simulated (Vignon et al., 2018) than in version AP. Figure 3 shows how version AP and 6A perform in a single-column configuration used to simulate the test case of DIurnal land-atmosphere Coupling Experiment (DICE) (Kansas, latitude 37.65°N, longitude 263.265°E) far from the ice sheets regions. The simulations cover a period of 3 days and three nights and the last night which is stable, and cloudfree is well suited to test the boundary layer scheme under stable condition. The hydrological scheme is bypassed by prescribing the ratio β of evaporation to potential evaporation and the surface thermal inertia to a value adjusted to the DICE case during the full run (Ait-Mesbah et al., 2015). For night time the near-surface temperature inversion is much stronger in 6A than for the AP run (Figure 3a). The sensible heat flux is reduced with the 6A version and closer to the observations than the AP version (Figure 3b), which produced a too strong vertical mixing.

3.2. Relative Impact of Atmospheric and Land Surface Components on the Biases of Near-Surface Variables

Most of the biases in evaporation, 2 m temperature, SW downward radiation at the surface, surface albedo, precipitation, and total precipitable water can be analyzed by inspecting zonal mean variables over the continents (Figure 4). To further comment regional aspects, maps of mean annual, JJA and DJF bias in 2 m temperature are depicted in Figure 5. The corresponding bias maps are displayed in the supplementary

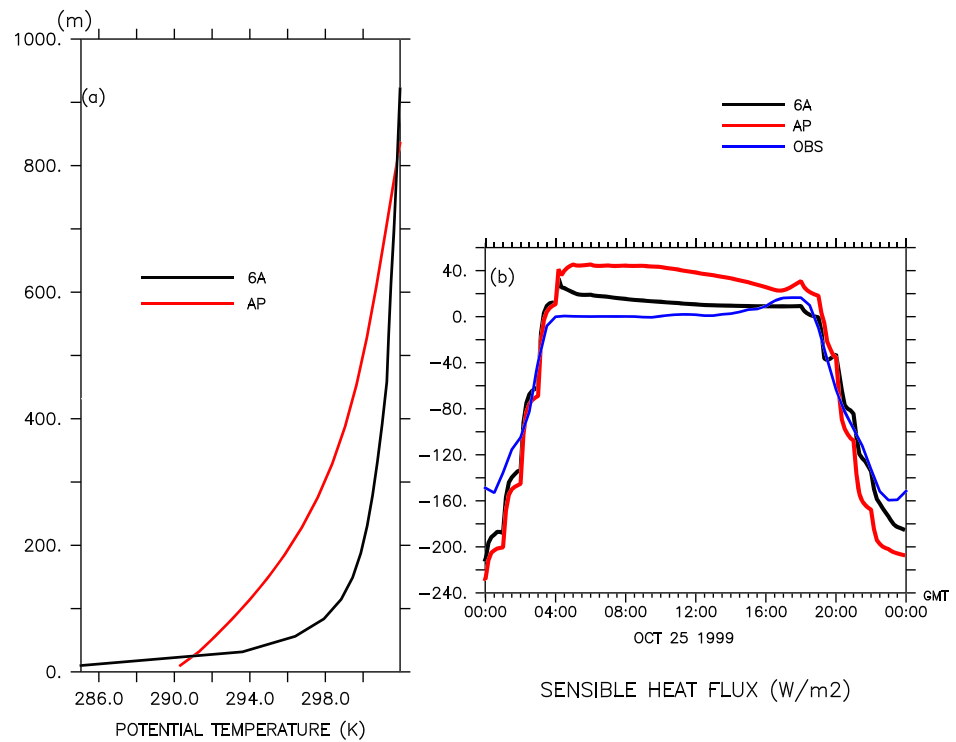


Figure 3. Temperature profile (a) and sensible heat flux (b) for the third night (stable) of the DICE case simulated with the AP (red) and 6A (black) version of the atmospheric physics. The observed sensible heat flux is plotted together with the simulations (blue).

information for the SW downward radiation at the surface (Figure S3), evaporation (Figure S4), surface albedo (Figure S5), precipitation (Figure S6), and total precipitable water (Figure S7). The maps corresponding to the first member of the AMIP ensemble are also plotted, in order to confirm the representativity of the 6Actrl experiment with respect to the AMIP published data. We verified that the features discussed hereafter are shared by the other members of the AMIP ensemble. The statistical significance of the changes caused by the new land surface and atmospheric physics is assessed geographically for each studied variable in Figures 6 (6Actrl-6Achoi) and S8 (6Actrl-APctrl), with very similar results to the differences maps for APctrl-APchoi and 6Achoi-APchoi (not shown).

A clear improvement of the CMIP6 reference configuration 6Actrl is related to the radiation budget. This improvement is illustrated by the reduction of the bias in the downward SW radiation at the surface in 6Actrl (Figures 4d and 4j) and can be attributed to the improvement of the representation of the Cloud Radiative Effect (CRE) coming from the modification in the parameterizations and to the improved tuning of the model free parameters targeting the CRE (Hourdin et al., 2020). Consistently with the overall reduction in the SW radiation bias (Figure S3) and in the evaporation bias especially over the continental United States (Figure S4) the strong warm bias over the midlatitudes in summer (Figure 5) that was shared by many models participating in CMIP5 (Cheruy et al., 2014) is reduced in the 6Actrl configuration used for CMIP6. Over the continental United States, Al-Yaari et al. (2019) also showed that the general agreement between areas of strong warm bias and areas of strong precipitation and soil moisture deficits is good. In the 6Actrl configuration the precipitation deficit is also significantly reduced (Figure S9) and the surface soil moisture is in better agreement with the observations (see section 4.1). In connection with the developments on the vertical diffusion scheme, the warm bias that extended over a large part of the polar and boreal regions in winter is reduced or even replaced by a cold bias over part of the Arctic continent and Ocean, Greenland, and Antarctica (Figure 5). The cold bias is probably overestimated over Greenland, the Arctic Ocean, and Antarctica due to a warm bias diagnosed in ERA-I (Jakobson et al., 2012; Reeves Eyre & Zeng, 2017; Vignon et al., 2018). When using ERA-5, as reference data set instead of ERA-I, the bias over Greenland is

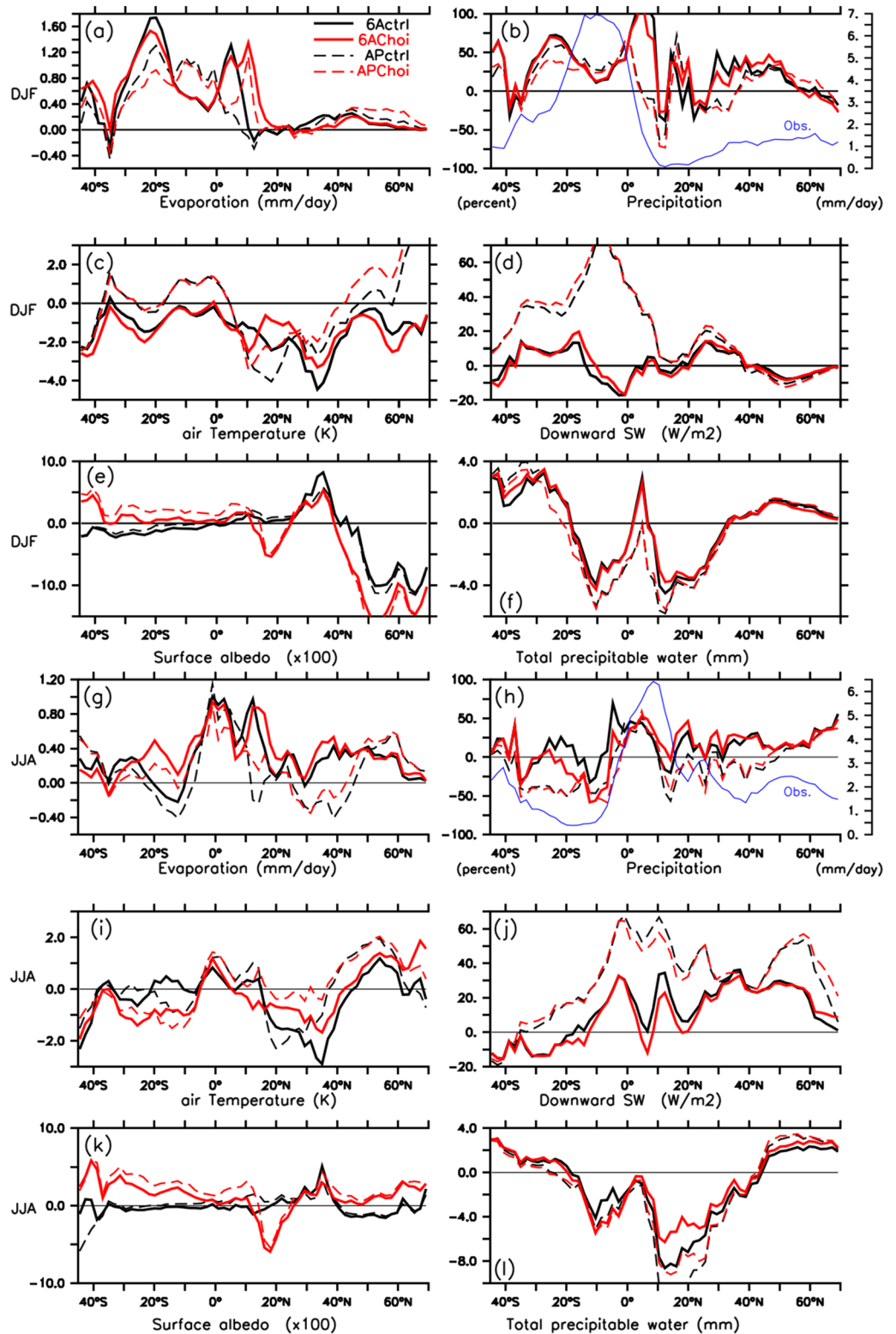


Figure 4. Zonal mean bias in December-January-February (DJF) and June-July-August (JJA) over continents for the evaporation (a, g), the precipitation (b, h), the air temperature (c, i), the downward shortwave (SW) radiation (d, j), the surface albedo (e, k), the total precipitable water (f, l) in 6Actrl (thick black curve), 6AChoi (dashed black curve), APctrl (thick red curve), and APChoi (dashed red curve). For precipitation the blue curve corresponds to the absolute value of the observations (y-axis on the right side). The references are described in Table 3.

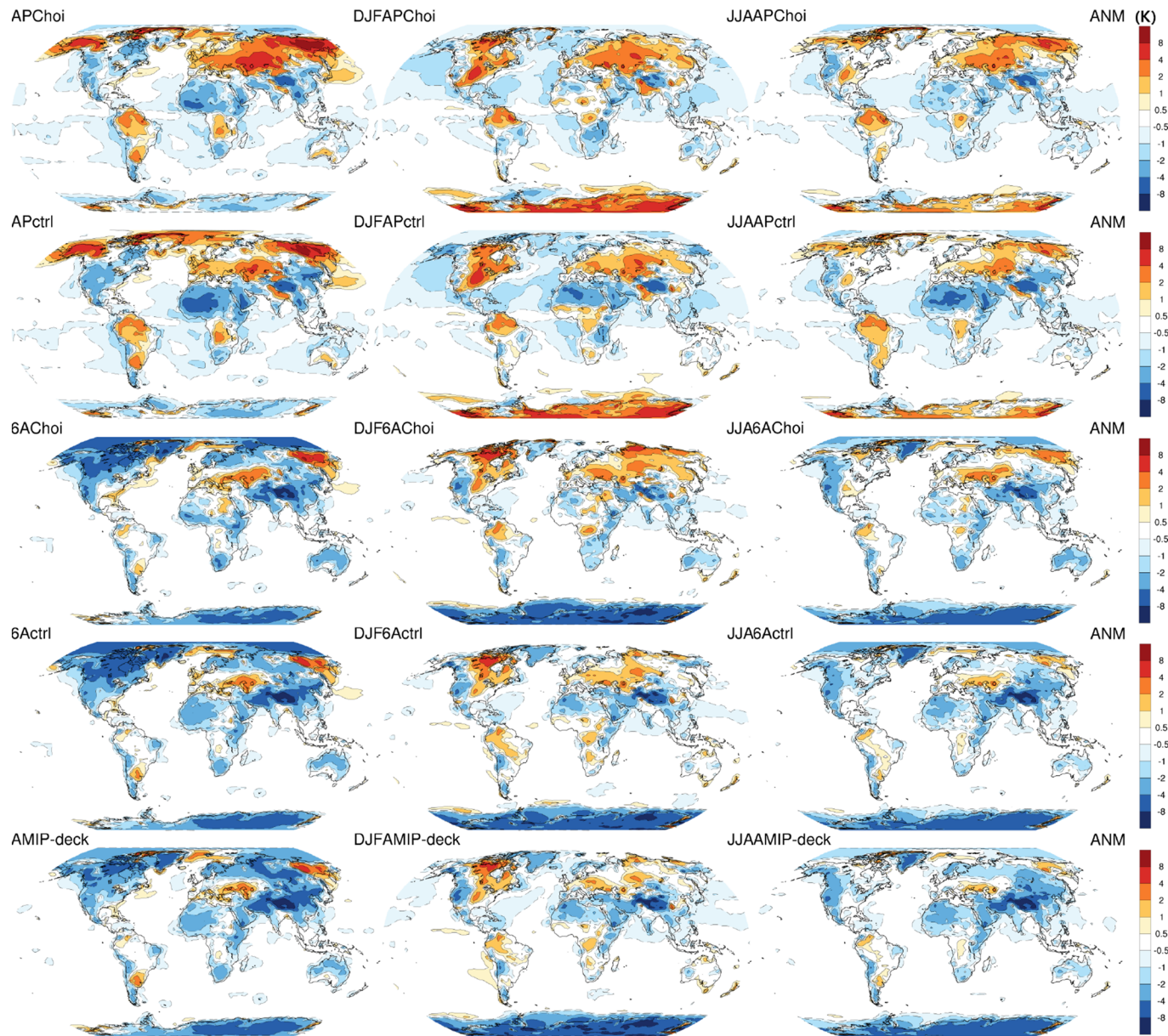


Figure 5. Mean multiannual bias in 2 m temperature (tas) for December-January-February (first column) and for June-July-August (middle column) and for the full year (last column) in the APChoi (first row), APctrl (second row), 6AChoi (third row), 6Actrl (fourth row), and AMIP configurations (fifth row). The reference is given by ERAI reanalysis averaged for the 1979–2014 period.

reduced in DJF (not shown). Over the Arctic continent Lindsay et al. (2014) report that ERA-I has a bias of less than 0.5 K compared to the observations.

As a result of the new snow scheme and of the optimization with respect to the MODIS observations, the surface albedo in the ctrl model is improved in most regions in winter (Figures 4e and S5) and over deserts (notably the Sahara) over the year. The new snow scheme improves the snow cover which was significantly underestimated with Choi (Figure 7). With the exception of the surface albedo and to a lesser extent the evaporation, the overall structure of the bias is only marginally sensitive to the land surface scheme whose impact is mostly relevant at the regional scale (Figures 5, 6, S3, S4, S5, S6, and S7).

When considering the continents globally, Choi and ctrl both overestimate the evaporation (especially in winter) regardless of the atmospheric model with which it is coupled. This overestimation is slightly less

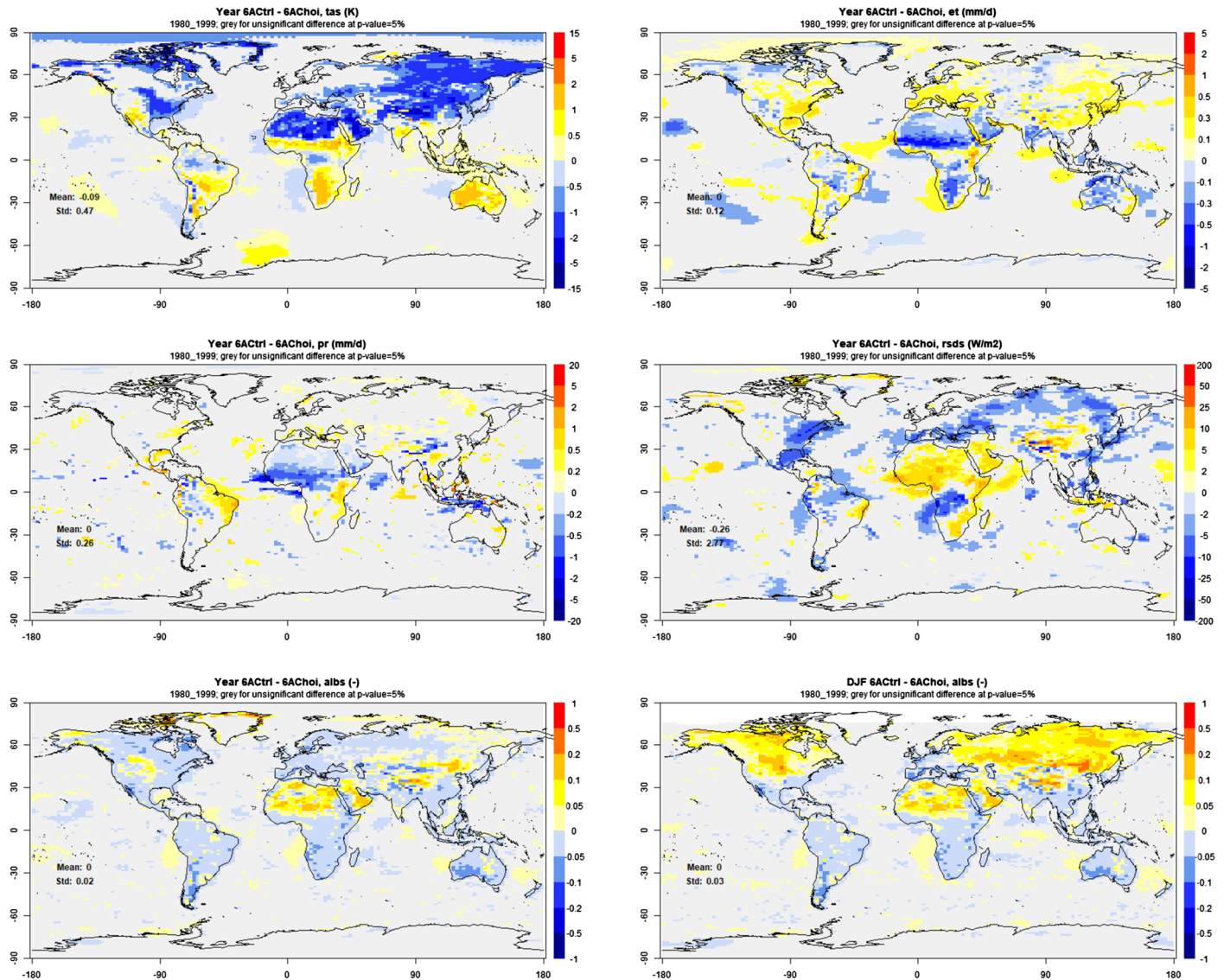


Figure 6. Significance of the multiannual differences between configurations 6Actrl and 6Achoi, with gray coloring where the difference is not statistically significant based on Student's t test (with a p value < 0.05). The first five maps show the yearly mean differences for the air temperature, evaporation, precipitation, downward SW radiation at the surface, surface albedo, and the bottom right map shows the winter (DJF) difference in surface albedo. The displayed means and standard deviations are calculated over the whole globe including non significant points.

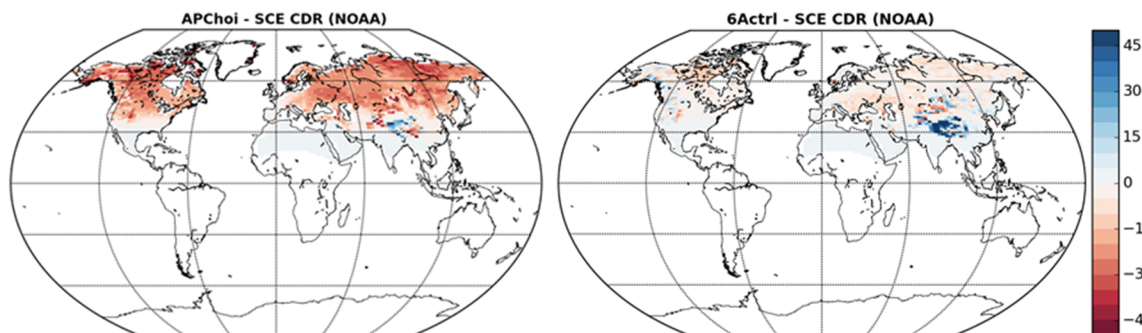


Figure 7. Mean annual bias in the snow fraction for the APchoi (left) and 6Actrl (right) configurations. The reference is taken from the NOAA Climate Data Record Snow Cover Extent diagnosed from the Interactive Multisensor Snow and Ice Mapping System at the National Ice Center.

Table 4
Mean Continental Biases in DJF and JJA for 2 m Temperature, Evaporation, Surface Downward Radiation, Albedo, and for the Reference Simulations (APChoi, APctrl, 6AChoi, 6Actrl)

Experiment	2 m T (K)	Evaporation (mm/day)	Precipitation (mm/day)	sfc SW (down) (W/m ²)	albedo (×100)
DJF					
APChoi	0.19	0.33	0.41	16.4	−0.83
APctrl	−0.39	0.30	0.47	15.2	−0.72
6AChoi	−1.40	0.36	0.57	1.07	−0.33
6Actrl	−1.47	0.34	0.58	0.63	−0.29
Obs	279.4	0.99	1.82	155.4	17.2
JJA					
APChoi	0.31	0.18	0.03	36.5	1.73
APctrl	0.05	0.11	0.03	35.8	0.19
6AChoi	−0.15	0.36	0.42	14.2	0.89
6Actrl	−0.37	0.28	0.37	16.27	0.01
Obs	293.8	1.75	2.06	227.5	18.

Note. APChoi corresponds to the IPSL-CM5A configuration used for CMIP5, and 6Actrl corresponds to the IPSL-CM6A configuration used for CMIP6. The last line corresponds to the mean value over continents calculated with the observation described in Table 3.

for ctrl (Table 4), albeit this result is modulated at regional scale (Figure 6). Investigating the minimum and maximum daily temperature shows a widespread warm bias of daily minimum temperature over the midlatitude (Figure 8). This bias is present over the whole year for the AP physical package used for CMIP5, and only in JJA for the 6A package used for CMIP6, it is very marginally sensitive to the land surface scheme. This is consistent with the reduction of the turbulent mixing in the PBL for the stable boundary layers obtained with the 6A atmospheric physics and with the results of Wei et al. (2017), which suggested that a bias in the simulated PBL mixing could very likely contribute to the temperature bias common to most of the models that participated to CMIP5 with AMIP experiments. The moist atmospheric bias over the midlatitudes in JJA (Figure 4l) could contribute to the warm bias of daily minimum temperature by minimizing the nocturnal radiative cooling, but further investigation is needed to explain this bias, which is shared by other models participating in CMIP6.

3.3. Atmospheric Process Sensitivity to the LSM Choice

The above analysis has shown that, for most variables and skills considered, the changes due to the atmospheric physics are larger and more broadly significant than the ones due to the land surface physics, as confirmed by the comparison between Figures S8 and 6, respectively. We

detail here the sensitivity of the 6A atmospheric physics to the LSM choice (Figure 6). The differences between 6AChoi and 6Actrl are statistically significant (at the 5% level) over most of the continents for all variables but precipitation. The seasonal differences (not show but for winter surface albedo) are very consistent with the yearly differences. Ctrl induces a significant cooling over an extended region going from Siberia to China (up to 3 K locally in absolute value). This cooling is accompanied with an increase in evapotranspiration, some local reductions of the downward SW radiation, but also a widespread decrease of surface albedo (mostly driven by the summer season thus by vegetation), which is probably overruled by the large increase in albedo in winter. In contrast, large land areas of the southern hemisphere exhibit a significant warming from Choi to ctrl, along with an evaporation decrease, a decrease in surface albedo, and a downward SW radiation increase. Two exceptions can be isolated to the cooling/warming response to evaporation increase/decrease. The first one is the Sahara, where air temperature is reduced with ctrl, despite significant reduction of evaporation and increase of incoming SW radiation: The reason is the substantial albedo increase in this area, like in most sparsely vegetated zones. The second exception comprises the humid equatorial areas (intertropical convergence zone), where surface air temperature decreases without any significant evaporation change: There, the main driver seems to be the reduction of incoming surface radiation, likely related to precipitation increases, although these changes are rarely significant, and mostly in JJA. Precipitation is also significantly impacted by the choice of the LSM over monsoon regions, like Western Africa in JJA and Southern Amazonia in DJF, where ctrl tends to reduce evaporation and precipitation. The few spots over tropical oceans where the change in precipitation and evaporation are significant are probably due to slight modifications of the circulation in response for instance to the temperature changes. However, the amplitude of the changes is very low with respect to the typical oceanic values in those regions. When considering the continents globally, Choi and ctrl both overestimate the evaporation (especially in winter). This overestimation is slightly less for ctrl (Table 4), albeit this result is modulated at regional scale (Figure S4).

3.4. Sensitivity Experiments

In order to further interpret the above results we use the sensitivity experiments described in Table 2.

Sensitivity simulations to the strength of the decoupling in stable condition were performed by changing the values of the minimal mixing length (l_{mixmin}) and of the critical Richardson number (ric) above which the stability functions of the turbulent diffusion coefficient reach their lower-bound value (see Figure 2 in Vignon et al., 2017 for details). Those two thresholds enhance the mixing and prevent the turbulence cutoff in very stable conditions (Table 2, 6Aric, 6Aric83lmx). Figure 9 shows the impact of the sensitivity

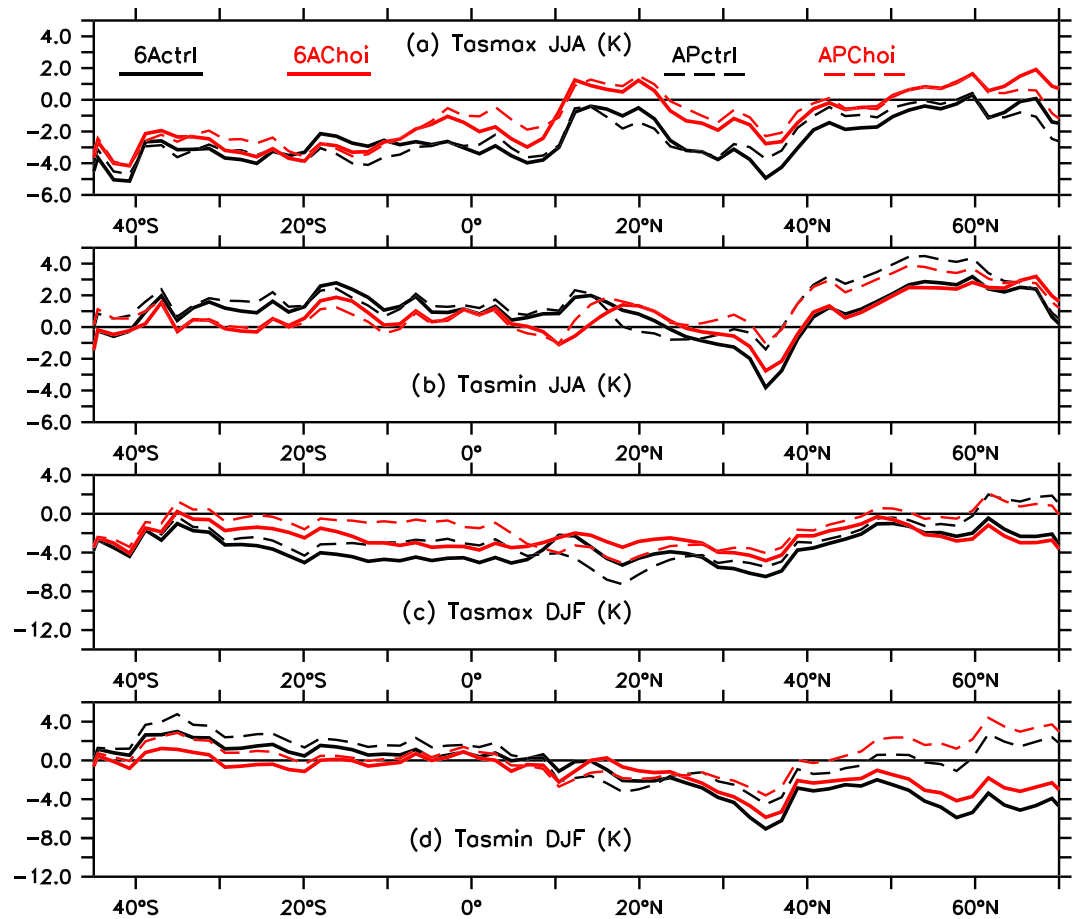


Figure 8. Zonal mean bias over continents in the seasonal means of minimum and maximum daily temperature for the reference configurations (thick black curve: 6Actrl, dashed black curve: 6Achoi, thick red curve: APctrl, dashed red curve: APchoi).

experiments on the zonal means in JJA and DJF. North of 60°N, the near-surface temperature is highly sensitive to these thresholds. Allowing less decoupling (Table 2, 6Ari83lmix) significantly reduces the cold bias over continental areas in winter, but it deteriorates the vertical temperature gradient over the Antarctic Plateau shown in Figure 2. A further increase of the decoupling with respect to the configuration adopted for CMIP6 (Table 2, 6Aric) leads to a reduction of the winter-time minimal temperature but does not impact the night-time bias in summer for the 6A version (not shown).

As expected, the orography-induced TKE production (Table 2, NoOro, also see Appendix A) tends to warm the midlatitude and boreal-latitude in winter which partially counterbalances the effect of the reduced vertical diffusion for the stable boundary layers (not shown). The impact of deactivating the drag induced by the vegetation penetrating the boundary layer (Table 2, NoTree) is negligible for the near-surface temperature (not shown).

A sensitivity simulation focusing on the evaporation for the ctrl model was also designed to target the bare soil evaporation, which can reach the potential rate when the moisture in the first four layers of the soil is higher than the residual moisture (Table 2, 6Arsol). It is likely that the potential rate of evaporation leads to an overestimation of evaporation when patches of soil begin to dry out in the grid cell. To overcome this defect a resistance to bare soil evaporation can be added to the aerodynamic resistance. This approach has been implemented in ORCHIDEE using the formulation proposed by Sellers et al. (1986). The activation of this option reduces the evaporation (Figures 9a and 9g). However, amplifying the SW radiation bias at the surface over the midlatitude north (Figures 9d and 9j) and reducing the evaporative cooling results in

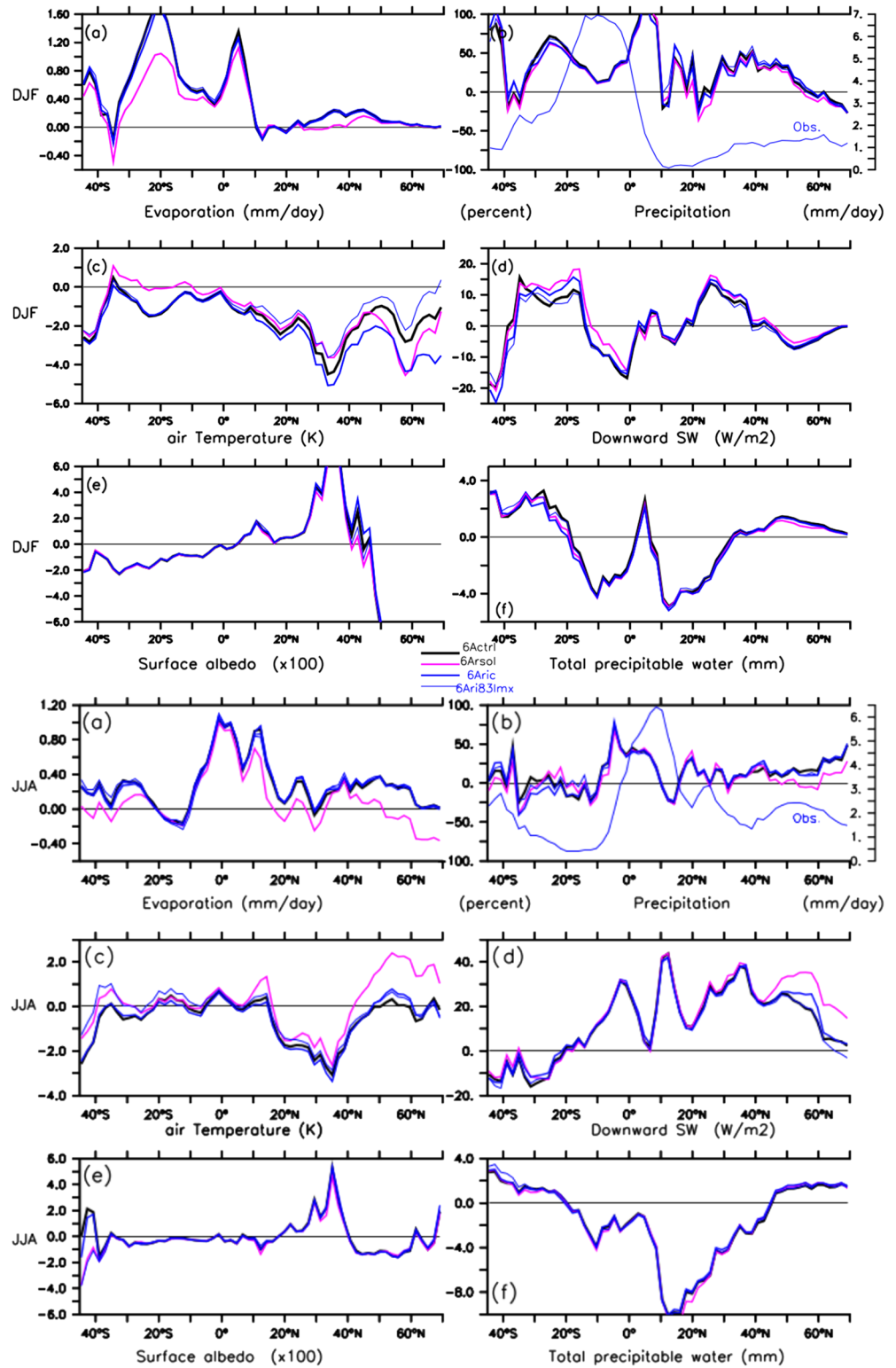


Figure 9. Zonal mean bias in DJF and JJA over the continents for the evaporation (a, g), the precipitation in percent and the absolute value of the observation (b, h), the air temperature (c, i), the downward SW radiation at the surface(d, j), the surface albedo (k, e), the total precipitable water (f, l) in the reference experiment 6Actrl (thick black curve), in sensitivity experiments for the turbulent mixing 6Aric (thick blue curve), in 6Aric83lmx (blue thin curve), and in sensitivity experiment with a resistance to bare soil evaporation activated (thick pink curve).

a strong warm bias (Figure 9c and 9i). The impact of deactivating the dynamical roughness height (Table 2, noz0Su) is detected at the regional scale on the evaporation and the temperature, but it is quite limited for the considered space and time scales (not shown).

3.5. Specific Regional Changes

Several biases mostly rely on regional features and are discussed in this section.

- *Sahara*: The cold bias between 15°N and 30°N in all simulations and for all seasons (Figures 4c and 4i) is mostly the signature of a cold bias over the Sahara (Figure 5). It may be due to aerosol specification or to the failure to consider emissivity lower than the unit in the radiative transfer calculations. The cold bias is less pronounced with the AP physics because the strong positive bias in the downwelling SW radiation and the underestimation of the surface albedo compensate the excessive surface cooling due to the overestimated value of the surface emissivity.
- *Tibetan Plateau and High-mountain Asia*: There is an overall cold bias in winter between 30°N and 40°N (Figures 4i and 5), which is particularly strong over the Tibetan plateau and High-mountain Asia where it is associated with a surface albedo bias (Figure S5) and an overestimation of the snow fraction (Figure 7). The albedo bias is not present in ORCHIDEE stand-alone simulations (not shown) and is lower when the old snow scheme is activated. This is consistent with a difficulty of the land-atmosphere model to melt snow leading to a too high albedo inducing a positive feedback on the temperature because of a deficit in net SW radiation at the surface. The weaker bias produced by the old snow scheme is consistent with the underestimation of the snow albedo, which was already documented by Wang et al. (2013). These results confirm that land surface atmosphere feedbacks play a significant role in this region. The temperature and the albedo biases are weaker in the HighResMIP simulations (not shown) and in nudged simulations (Figures S10 and S11). The weakening of the bias obtained with the increase in resolution or with the wind nudging confirms that the regional circulation is an important component of the High-mountain Asia climate. A high resolution allows us to represent more realistic contrasts of the snow cover between the lowlands and the high mountains. It is also a way to better simulate the role of the orographic barrier played by the High-mountain Asia that stops the northward transport of moisture originating from the Indian subcontinent. This barrier explains the dryness of the Tibetan plateau (Krishnan et al., 2019; Ménégoz et al., 2014; Sabin et al., 2013), where an excess of moisture flux is simulated at coarse resolution, inducing a positive bias of snow cover that is enhanced by surface feedback. In the same way, by correcting the regional circulation, the nudging can reduce the positive bias of snow cover which impacts the surface albedo.
- *Central Asian lowlands*: The more realistic representation of the snow albedo and the increased decoupling for stable boundary layers help obtain more realistic near-surface temperatures but does not eliminate the strong warm bias present in winter on the Central Asian lowlands in CMIP5 (Figure 5, DJF). The temperature bias is further reduced when the large-scale circulation is relaxed toward meteorological analysis. The nudging reduces also the total precipitable water (not shown) that is greatly overestimated in this region. These results suggest that the large-scale dynamics contribute to the bias by a too strong moisture advection, the latter limiting radiative cooling. A residual negative bias in surface albedo (Figure S5 DJF) can also contribute to the warm bias. In summer, the warm bias is also present, but it is mainly associated with an excess of SW radiation at the surface.
- *Eastern Siberia*: Regardless of the model version, a strong warm bias persists in the extreme north-east of Siberia, north of the Sea of Okhotsk, and north of the Bering Sea. The bias is not present in the nudged-by-wind simulations (Figure S9), and it is less marked when the new snow scheme and the soil freezing are activated (NoSnowFreez experiment in Table 2, not shown). The bias is also reduced when the decoupling is increased. This suggests that both large-scale circulation and local processes and their interactions play a significant role in this region.
- *Southern Great Plains*: While substantial biases are reduced with respect to the APChoi configuration of the model used for CMIP5, a warm bias remains over the Southern Great Plains. The Clouds Above the United States and Errors at the Surface (CAUSES) experiment (Morcrette et al., 2018) in which IPSL participated highlighted a strong deficit of deep-cloud events (reduced in the CMIP6 version with respect to the version that participated in the intercomparison; Kwintin Van Weverberg, personal communication). Concerning the precipitation, Van Weverberg et al. (2018, their Figure 13) show that none of the models

that participated in CAUSES are able to correctly represent the diurnal cycle of the precipitation evaluated with the Atmospheric Radiation Measurement Best Estimate (Xie et al., 2010). The nudging does not allow to reduce the bias. In this region, rainfall comes from two different convective regimes. The first regime is associated with a local triggering of convection induced by daytime heating, and the second regime corresponds to the propagating systems over the Great Plains, initiated in the lee of the Rockies (Klein et al., 2006). The precipitation associated with the first regime is fairly well represented by the LMDZ model with a maximum delayed in the afternoon, which is a robust improvement of the convective scheme (Hourdin et al., 2020; Rio et al., 2009). The night-time maximum due to propagative systems is absent in most models of CMIP5/CMIP6 and in particular in the simulations of LMDZ, which has no parameterization for this type of propagative system.

- *Amazonia and Central Africa*: The strong warm bias present in the simulation with the AP atmospheric physics does not exist in the simulation with the 6A physics (Figure 5) as a result of the strong reduction of the downward SW radiation at the surface discussed in section 3.2.

3.6. Tuning of the Global Model and Near-Surface Temperature Over Land

Significant efforts have been made to improve the physical content of the parameterizations. Yet, they remain an idealized and approximate representation of processes. As a consequence adjustment and tuning are unavoidable when all the atmospheric, land surface, and oceanic components are coupled (Hourdin et al., 2017).

A tuning of subgrid scale orography (SSO) was performed to better represent the atmospheric heat transport toward the Arctic Ocean, which is a key region for sea-ice formation and melting. The SSO schemes are applied to represent the blocking effect of orography at low levels and the breaking of gravity waves (see Lott, 1998 and more details in Appendix A). The sensitivity experiments (Table 2) reveal that the SSO tuning has an impact on the near-surface temperature mostly during the cold season, from November to March (see Figure 10), which is consistent with the established impacts of orography onto the large scale atmospheric circulation (Holton, 2004). Increasing the blocking effect of orography through the drag scheme cools Eurasia and warms western North America. This is consistent with a large blocking effect over the Rockies when increasing the drag, inducing anomalous southerly warm advection upstream, and northerly cold advection downstream (Holton, 2004). The sensitivity to the lift that modifies the flow direction shows different effects, with warm anomalies upstream of the Rockies and Himalayas and cold anomalies downstream of the Rockies and Himalayas, but with a larger amplitude, different location, and with a zonal-wavenumber 2 structure. The lift effect results from applying a force perpendicular to the local flow over orographic barriers. It causes larger meridional flow anomalies than the drag, which explains the stronger impact in terms of surface air temperature. The tuning of the version 6A was mainly done by increasing the drag and slightly reducing the lift parameter so that the tuning may have contributed to enhance the cold bias over Siberia, while reducing it over North America. However, the temperature anomalies explained by the new tuning remain small when compared to the bias itself.

An essential aspect of the tuning is to ensure that the radiative budget at the top of the atmosphere is in equilibrium and that the latitudinal distribution of each component of the radiative budget is as close as possible to the observations. A particular care was given to the tuning of free model parameters impacting the top of the atmosphere (TOA) radiative budget (Hourdin et al., 2017). Interestingly, none of the sensitivity studies described above strongly impacted the TOA radiative budget. This indicates that specific tuning targeting the land surface processes can be done independently to some extent. Such an approach has not been adopted for the 6A version of the IPSL-CM, but it could improve the performances of the model and reduce some bias in future versions of the model (Li et al., 2019).

4. Improvement of the Realism of the Hydrological Cycle in the Coupled Continental Surface-Atmosphere System

The impact of the more physical hydrological scheme (ctrl) used for CMIP6 (section 2.2) and the impact of the more realistic convective precipitation documented in Hourdin et al. (2020) on the hydrological cycle are addressed in this section in two specific ways: the analysis of moisture and energy coupling at the surface at regional spatial-scale and monthly time-scale and the analysis of the seasonal cycle of precipitation and river discharge at the scale of individual watersheds.

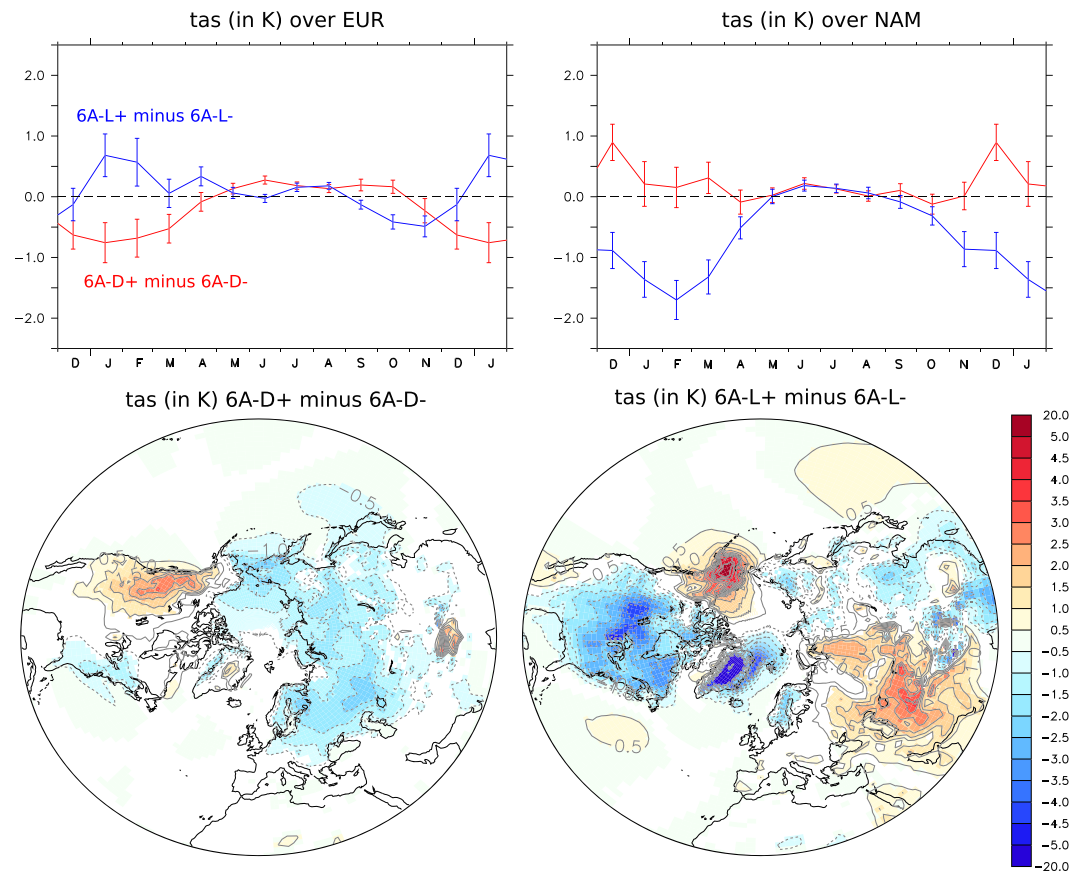


Figure 10. Top panel: 2 m temperature (CMIP6 variable tas) anomalies (in K) induced by the drag and lift parameters over (left) Eurasia (EUR, 20–80°N, 10°W–180°E) and (right) North America (NAM, 20–80°N, 180–10°W). The blue line indicates the difference between 6A-L+ and 6A-L-. The red line indicates the difference between 6A-D+ and 6A-D-. Bottom panels: surface air temperature anomalies (in K) induced by the (left) drag and (right) lift parameters in the Northern Hemisphere. Colors are shown only for significant areas (p value of Student t test lower than 10%).

4.1. Soil Moisture-Evaporation-Radiation-Precipitation Coupling

The impact of the modified parameterizations on surface soil moisture, net SW radiation at the surface, evaporation, and precipitation is documented at regional scale in order to ensure homogeneous climate conditions to prevail. We focus on two hotspot regions (Koster et al., 2004) where the soil moisture-atmosphere coupling is strong: the Central North America (CNA) region as defined in the Special Report on Managing the Risks of Extreme Events and Disasters to Advance Climate Change Adaptation (SREX) (Seneviratne et al., 2012) and a box in the Sahel (–10, 30°E, 0–20°N). A third region corresponding to Western Europe (WE) where the coupling is weaker is also considered. The grid points corresponding to the WE box are selected according to the *KoepfenGeiger* climate classification system (Kottek et al., 2006) (Region 21 in Figure S12).

For these regions, combined distributions of soil surface moisture, evaporation, net radiation at the surface, and precipitation for the four reference configurations (6Actrl, APctrl, APChoi, 6AChoi) and for different sets of observations (Table 3) are constructed based on monthly values for a 10-year long period in which all observations are available (2001–2010).

First considering the distribution for the simulated surface soil moisture itself, the regional histograms of the surface soil moisture show that the Choi land surface hydrological scheme produces a very narrow distribution with unrealistic null value of the surface soil moisture for lower boundary and low maximum values of the surface soil moisture (not shown). These characteristics of the surface soil moisture with the Choi scheme can be explained by the crude representation of the hydrology by this scheme for which the

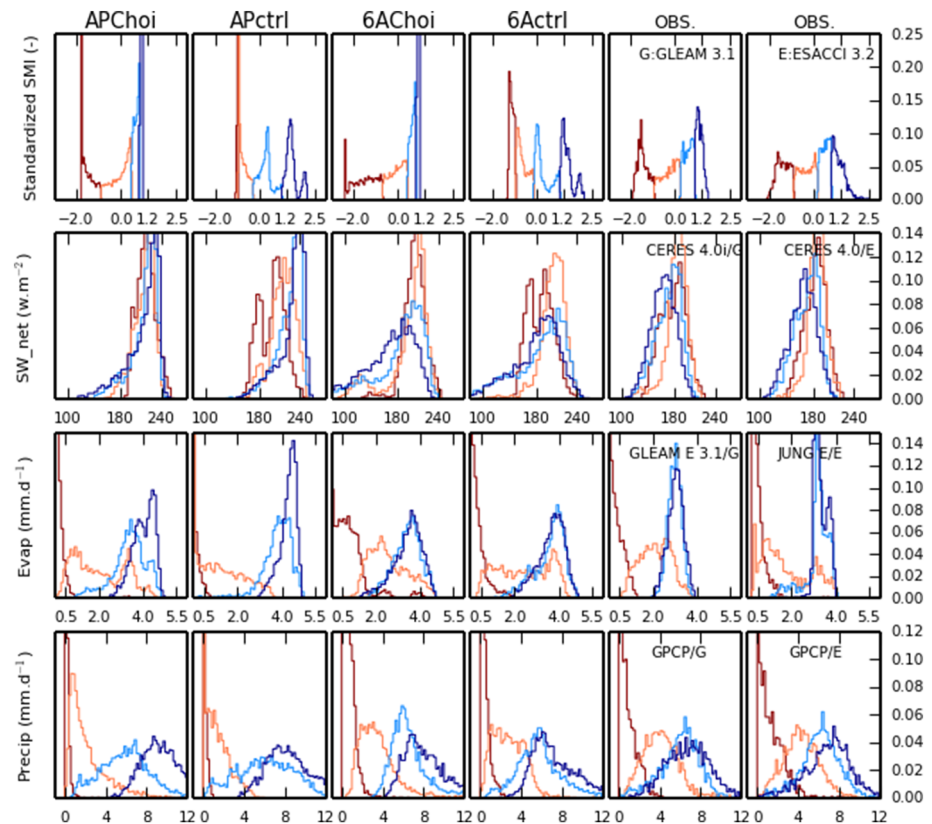


Figure 11. Regional histograms computed from monthly values of the individual grid points corresponding to the Sahel box ($-10:30^{\circ}E, 0:20^{\circ}N$) in JJA. The histograms are constructed for a 10-year long period in which all observations are available (2001–2010). Each row is dedicated to a particular variable: surface standardized soil moisture (first row), net SW radiation at the surface (second row), evaporation (third row), and precipitation (fourth row). The first four columns correspond to the reference experiments, and the last two columns correspond to the different sets of observations indicated above the corresponding histograms. The colors depict the PDF from the minimum to first quartile (dark red) from first quartile to the median (pale orange), from median to third quartile (cyan line), and from the third quartile to the maximum (blue line). For soil moisture, the y-axis is cut at .25 (representing 25% of the quartile) for the sake of readability but the driest quartile peaks at 0.8 (corresponding to 80% of the quartile) for APctrl and the moister quartile peaks at .8 for APChoi and APctrl. For evaporation they-axis is cut at .14 (corresponding to 14% of a quartile), but 55% (APChoi) and 90% (APctrl) of the evaporation associated with the first quartile is less than 0.1 mm/day. For the precipitation, the y-axis is cut at .12, but 70%, 85%, 15%, and 40% of the precipitation associated with the driest soil moisture quartile are less than 0.1 mm/day for APChoi, APctrl, 6AChoi, and 6Actrl and 20% and 10% for GLEAM and ESA-CCI.

surface layer exists only intermittently. When considering the GLEAM and ESA-CCI soil moisture products, the width of the distribution is significantly smaller with the ESA-CCI product than with the GLEAM product (not shown). The fact that GLEAM takes the upper 0–10 cm into account while ESA-CCI correlates better with soil moisture up to 5 cm depth (Dorigo et al., 2017) while the surface soil moisture in the simulations corresponds to the moisture in the top 10 cm of soil might contribute to the differences. In addition, GLEAM and ESA-CCI soil moisture products are considered as observations, but they are highly dependent on the underlying models used to produce them and therefore suffer limits identified by Koster et al. (2009) that call for great caution regarding the reliability of the absolute values retrieved. For these reasons we prefer using the standardized Soil Moisture Index (SMI) defined in R. D. Koster et al. (2009; see their Equation 1), and the soil-moisture information at monthly time scale is mostly used to discriminate between very dry, moderately dry, moderately moist, and very moist soils in the corresponding regional distributions for evaporation, net SW radiation at the surface, and precipitation.

For soil moisture in the Sahel region (Figure 11) the summer observations feature a U-shaped distribution in which dry and saturated states prevail. This U-shaped distribution is reproduced by both schemes (Choi and

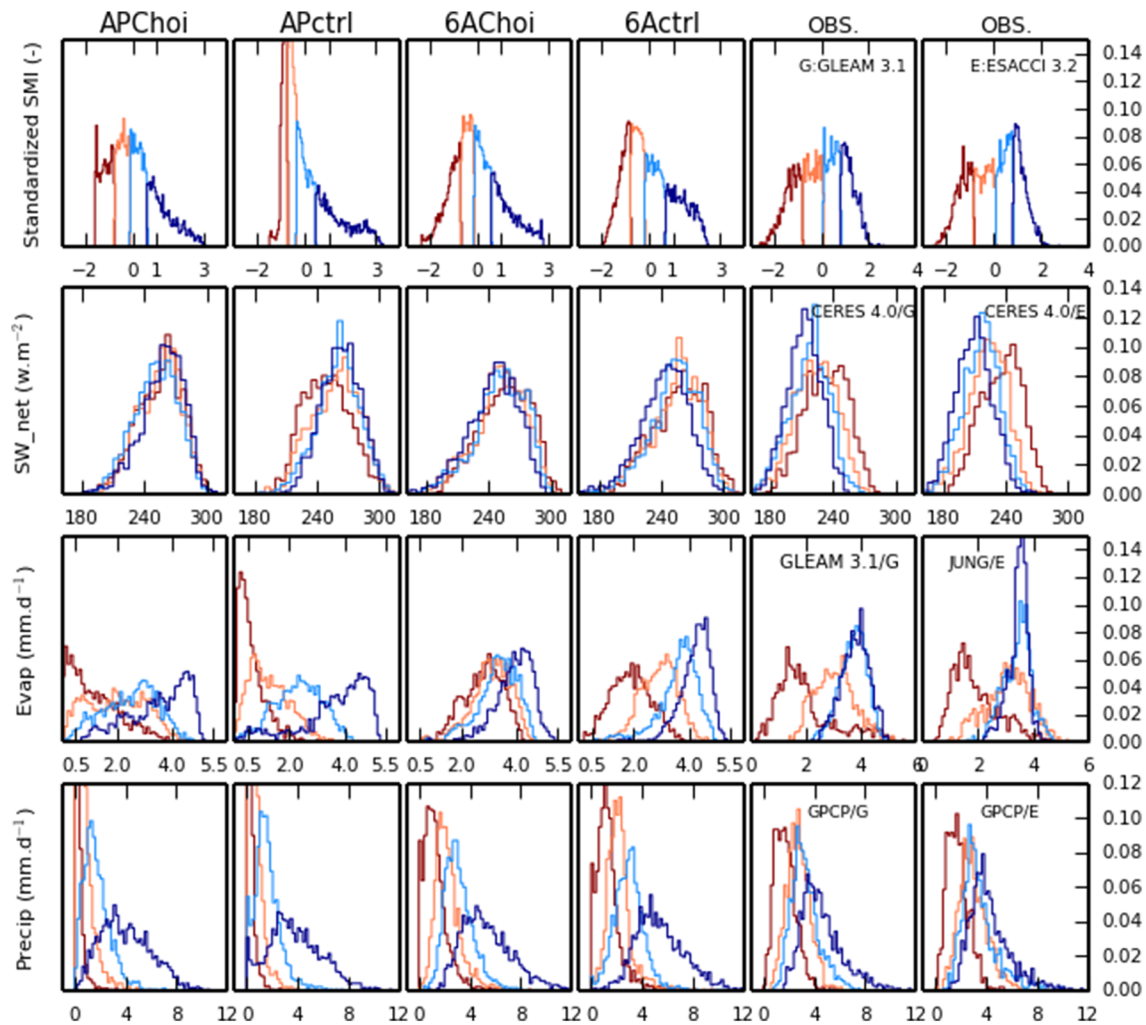


Figure 12. Regional histograms computed from monthly values of the individual grid points corresponding to the SREX CNA region (Seneviratne et al., 2012) in JJA. The histograms are constructed for a 10-year long period in which all observations are available (2001–2010). Each row is dedicated to a particular variable: surface standardized soil moisture (mrsos, first row), net SW radiation at the surface (second row), evaporation (third row), and precipitation (fourth row). The first four columns correspond to the four reference experiments and the last two columns to the different sets of observations indicated above the corresponding histograms. The colors depict the PDF from the minimum to first quartile (dark red) from first quartile to the median (pale orange), from median to third quartile (cyan line), and from the third quartile to the maximum (blue line).

ctrl) with strong differences: Choi favors the moistest contents much more than the observations while ctrl leads to a tri-modal distribution. This feature has been observed for several other regions with different climate and is the signature of using one dominant soil texture among three possible ones in each grid cell of the region, while in reality, many different soil textures coexist and lead to a mixed behavior. However, the U-shape is also present indicating that the scheme tends to favor dry or saturated situations for each texture as well. For all regions, the highest value of the net SW radiation is overestimated by as much as 20 Wm^{-2} . This holds for both AP and 6A versions of the model and for each soil moisture quartile. Various hypothesis can be formulated: This bias can either rely on a difficulty in processing CERES observations to retrieve the net radiation at the surface or rely on LMDZ. In this case, a problem with the radiative transfer code or a lack of simulated clouds or an underestimation of their radiative impact can be invoked. For the Sahel, when the surface is moist, the 6Actrl configuration tends to underestimate the occurrence of situations with an elevated evaporation rate and overestimate the occurrence of situations with low values of the net SW radiation (second and third columns in Figure 11). This feature can be interpreted as a too frequent occurrence of radiation-limited evaporative regimes with

respect to the soil moisture-limited evaporative regimes in this region. For CNA and for AP physics radiation is either insensitive to soil moisture (APChoi) or the low radiation is surprisingly associated with the driest soil quartile (APctrl) while, for 6A physics, low radiation associated with extended cloud cover is rather associated with the wettest quartile, which is consistent with the CERES product. Over both CNA and Sahel and for the driest surface soil moisture quartile, AP tends to favor little or no rainfall at the monthly time scale, probably over-simulating dry events. This feature is much weaker with 6A physics and in better agreement with the observations (bottom row in Figures 11 and 12). When Choi hydrology is activated with 6A physics, dry soils tend to have a sustained rate of evaporation, while the 11-layer hydrology also allows low evaporation rates consistent with the observations. When AP physics is activated, dry soils tend to be associated with too weak evaporation rates, this feature being more pronounced with 11-layer hydrology. Additional information concerning the evolution of the performances of the atmospheric model in the Sahel with the AP and 6A atmospheric physics are given in Diallo et al. (2017). In the hotspot regions, the 6Actrl configuration used for CMIP6 is the closest to observations due to both improved atmospheric physics and representation of soil hydrology. Low precipitation rates (at monthly time-scale) associated with dry soil are also overestimated in Western Europe. In this region where the soil moisture-atmosphere coupling is expected not to be dominant, the simulated net SW radiation, the simulated evaporation, and the simulated precipitation appear to be more sensitive to the soil moisture than the observed ones (Figure S13).

4.2. Seasonal Cycle of Precipitation and River Discharge

Figure 13 shows the seasonal cycle of precipitation observed and simulated by the four sensitivity experiments described above for 14 major watersheds together with the seasonal cycle of the river discharge observed and simulated at 14 stations on the rivers of the same major basins. For four out of the five boreal basins (Yukon, McKenzie, Yenisei, and Lena) the precipitation is often overestimated in all configurations. For some basins including Mississippi, Congo, and Amazonia, the seasonal cycle of simulated precipitation is significantly improved in volume or in phase in the configuration used for CMIP6 (6Actrl). For instance, in Tocantins basin in the Cerrado, the duration of the dry season is now reduced in agreement with the observations. This improvement can be attributed to changes in the parameterizations of the atmospheric physics. The impact of the LSM is limited, except over some midlatitude basins such as the Danube where the volume of precipitation is controlled by atmospheric physics and continental hydrology and is overestimated with the 6Actrl configuration used for CMIP6. With the 6Actrl configuration, simulated river discharges are also improved for the Mississippi, Amazonia, and Congo, owing to improved precipitation volume. The seasonal timing of river flow is different from that of rainfall because of the time needed for water to circulate in soils and along river systems after it has reached the ground. This timing is usually correct, with errors resulting from those of the simulated precipitation (e.g., intensity and location of rainfall events inside the watersheds), simulated land surface processes (e.g., snowmelt dynamics, permafrost, and transit times in the soil), and the fact that residence times of the routing reservoirs only depend on the type of reservoir (stream, overland, and groundwater) and the grid cell slope, while other regional factors can be important. In particular, the absence of floodplains in all the simulations largely explains the overestimation of river discharge in the Niger (d'Orgeval et al., 2008) and Congo and may contribute to the early peak flows of the Amazon (Guimberteau et al., 2012). The parameterizations of the land surface processes have a major effect in the five Arctic rivers, with a higher flow and earlier maximum when ground freezing is activated. This effect improves the simulated discharge in the two basins with the largest fraction of permafrost (Yenisei and Lena, in eastern Siberia). In the other three basins (Ob, Yukon, and McKenzie), the extent of frozen soils may be overestimated, and the overestimation of the river discharge by 6Actrl can also be related to the lack of dams and floodplains in the model (Gouttevin et al., 2012), with a potential feedback on permafrost extent, since a stronger cooling is required to freeze a wet soil than a dry soil. The Brahmaputra (India) discharge shows improved volume and seasonality with the 6Actrl configuration, while the maximum of the precipitation is underestimated. For this particular river that originates from the Angsi glacier located in Tibet, the change in atmospheric physics improves the timing while the maximum discharge is improved (reduced) with the activation of the soil freezing. This nonintuitive impact of soil freezing is caused by an atmospheric feedback, with less precipitation in the watershed if the freezing is activated. Yet, the positive bias of all simulated discharges might rather be related to massive irrigation in this basin (Guimberteau et al., 2012), which is not taken into account in these simulations.

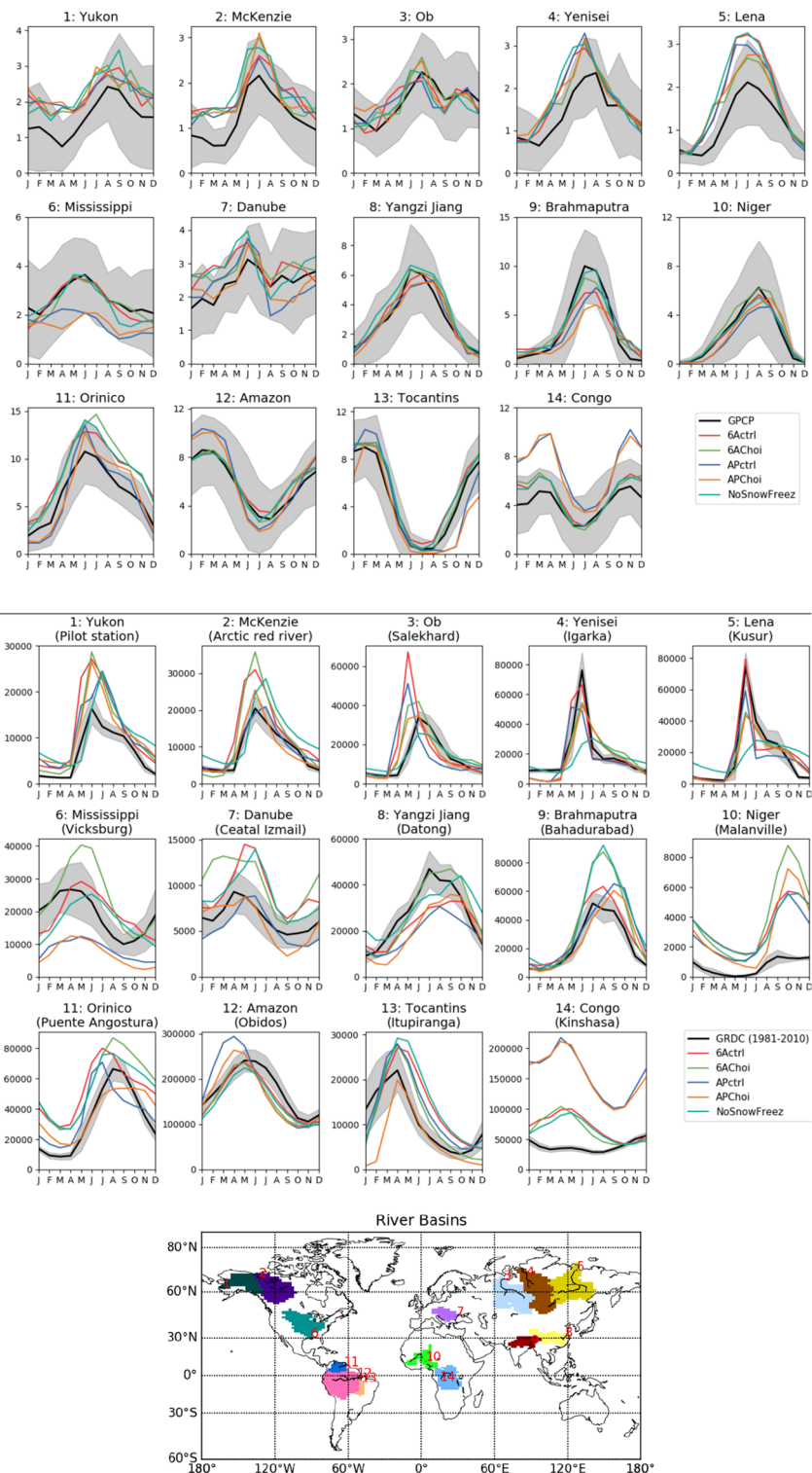


Figure 13. Multiannual mean seasonal cycle of the precipitation (upper panel) and of river discharge (lower panel) observed and simulated for 14 major river basins and for the four reference experiments: 6Actrl, Choi6A, APctrl, and ChoiAP and for the “NoSnowFree” experiment described in Table 2. The observations refer to the GPCP product for precipitation and to the Global Runoff Data Center (GRDC) database for the river discharges (Milliman & Farnsworth, 2011). The gray shaded areas indicate the interannual variability of the observed precipitation in the basin area (upper panel) and the interannual variability of the river discharge at the measurement stations.

5. Concluding Discussion

The quality of the coupled atmosphere-land continental surface system implemented in the IPSL-CM for CMIP6 is evaluated, and the relative role of atmospheric and land surface processes in controlling the coupling at the surface is analyzed and quantified. The following conclusions are reached:

- The improvement of the radiative balance and in particular the surface downward SW radiation makes it possible to reduce several temperature biases, some of which were shared by many models that participated in the CMIP5 exercise (e.g., summer bias in midlatitudes Stouffer et al., 2017). This confirms the essential role of the radiation and its interactions with clouds for continental climates.
- The temperature in the surface layer of the polar regions is significantly improved thanks to the refined turbulent diffusion scheme for stable situations and to the new longwave radiative scheme in LMDZ version 6A (Vignon et al., 2018). The boreal regions respond with a slightly excessive reduction of the daily minimum temperature while in CMIP5, several models including LMDZ shared a warm bias (Wei et al., 2017). A more detailed consideration of the turbulent mixing linked to the subgrid orography or high vegetation may help to partially compensate for this cooling, but further tests and evaluation are necessary.
- With the exception of the surface albedo, the snow cover, and to a lesser extent the evaporation, the overall structure of the near-surface biases is only marginally sensitive to the land surface scheme whose impact is mostly relevant at the regional scale. However, for a given description of the atmospheric physics, the differences induced by the change in the LSM are statistically significant (at the 5% level) over most of the continents for all variables examined but precipitation.
- The multilayer hydrology gives a representation of the surface soil moisture in better agreement with available observations than the Choi scheme, and the representation of evaporation in regions of strong coupling of the continental surface with the atmosphere is significantly improved.
- The snow scheme of intermediate complexity implemented in ORCHIDEE leads to a better description of the snow cover on the continents. Mountainous regions and in particular the Tibetan Plateau and High-mountain Asia remain challenging because radiative feedbacks and an imperfect description of the circulation in these regions at regional scale induce a strong cold bias. Further refinements of the snow scheme over complex terrains and of the atmospheric circulation are required to reduce these biases.
- The calculation of the fraction of frozen water in the soil implemented in the multilayer hydrology combined with the improved realism in volume and seasonality of the precipitation simulated with the 6A version of LMDZ has improved the seasonal cycle of rivers discharge in several major river basins.

Further developments based on the current version of the coupled atmosphere-land continental surface system are also identified:

- The attempt to take into account sources of turbulent mixing such as orography-induced small scales gravity-wave drag (Steenefeld et al., 2008) or the drag induced by vertical obstacles penetrating the boundary layers such as trees needs to be further refined.
- The benefit of using the dynamical roughness lengths as proposed by Massman (1999) and tested locally by Su et al. (2001) over homogeneously vegetated surfaces (shrub, cotton, grass) has still to be thoroughly evaluated in the context of the imperfect heterogeneous land-atmosphere coupling. In this context, the bulk formulae for flux calculation use a unique value of the roughness length, aggregated over possibly highly heterogeneous subgrid surfaces, and a potentially wide range of contrasting subgrid surfaces sees the same boundary layer properties. The development of more robust parameterizations for flux calculation over heterogeneous surfaces could benefit in the future from high-resolution simulations such as Large Eddy Simulations.
- For CMIP6, even though it would have reduced an overall overestimation of the evaporation, we considered it preferable not to activate the evaporation resistance of the bare soil in its current state to avoid reinforcing a warm bias in summer that would affect the quality of the simulations. Further work is needed to better calibrate the intensity of the evaporation resistance, which also impacts the ratio of transpiration to total evapotranspiration, shown to exert a key influence on biophysical feedback strength in both present and future climates (Zeng et al., 2017). Owing to the number of intricate parameterizations in a CM, such work cannot be done in isolation, and our results show that particular attention must be paid to the uncertainties of cloud parameterizations and cloud-radiation interactions.

- The multilayer hydrology enables to consider new developments for the CM. One of them is the introduction of realistic groundwater description, which may alleviate some biases by means of enhanced evapotranspiration owing to capillary rise from the water table (Campoy et al., 2013; Wang et al., 2018). The inclusion of irrigation in the simulations could also help reducing persistent biases (Puma & Cook, 2010), especially in places where it is fed by groundwater abstraction at non-renewable rates, like in India or the U.S. Great Plains (Al-Yaari et al., 2019; Famiglietti, 2014).
- In the version of ORCHIDEE used for CMIP6, the soil freezing is diagnosed in each soil layer, but the latent heat release/consumption associated with water freezing/thawing is not accounted for. This is, together with the better description of soil organic matter decomposition (Guimberteau et al., 2018), a preliminary step to account for the biogeochemical implications and positive feedback to global warming due to permafrost disappearance.
- Since the CMIP6 version, a description of the nitrogen cycle and its coupling to the carbon cycle has been implemented in ORCHIDEE (Vuichard et al., 2019). The impact of soil nitrogen availability (and more generally of soil nutrients) is crucial for plant growth but also for the energy and water cycle. Very recently we also included an ensemble of developments to improve the representation of forest dynamic and forest management with the inclusion of (i) a new canopy radiative transfer scheme (two streams model), (ii) a new carbon allocation scheme based on observed allometric relationships, and (iii) age and diameter classes and management practices (from natural to coppices). These developments described in Naudts et al. (2015) have a direct impact on the surface climate, changing the albedo of forest, the roughness length (varying with tree height dynamic), the latent and sensible heat fluxes, and the overall surface temperature (see an application over Europe in Naudts et al., 2016).
- Interestingly, none of the sensitivity tests to the surface processes described in this paper significantly impacted the TOA radiative budget, an essential target of the tuning of global CMs. This indicates that there is latitude for independent tuning for TOA radiation and for the land surface processes. Such an approach has not been adopted for the 6Actrl version of the IPSL-CM, but it could improve the performance of the model and reduce some bias in future versions of the model (Li et al., 2019). The tuning of the free parameters is now recognized as necessary step in model development (Hourdin et al., 2017) that should not rule out the improvement of the physical content of parameterizations.

Appendix A: Gravity-Wave and High-Vegetation Drag Induced TKE

LMDZ deals with two effects of the subgrid orography on the atmospheric flow:

1. the orographic blocking effect (called drag),
2. the orographic effect on the wind direction (called lift).

The drag and lift effects are described in Lott (1999). These two effects were modified during the tuning process (Gastineau et al., 2020). The drag and lift parameterizations (Lott & Miller, 1997) encompass two processes: (i) the “blocking” of the flow leading to a flow separation at the relief flanks and (ii) the orographic gravity-wave drag. The latter accounts for the drag due to wave breaking in the middle atmosphere as well as for the drag induced by low-level dissipation and breaking of trapped lee waves (Lott, 1998). The drag effect is calculated applying a local force opposed to the local flow, and it is used in all CMs (Sandu et al., 2019). The lift effect is less widely used and involves a force perpendicular to the local flow.

For the setup of the sixth version of the model, the effect of the drag exerted by vegetation protruding into the first model layers has also been parameterized in LMDZ following Nepf (1999) and Masson & Seity (2009).

Orographic gravity-wave breaking and dissipation (e.g., Epifanio & Qian, 2008; Sun et al., 2015) as well as flow-canopy interactions (Finnigan, 2000) have been shown to be common paths to turbulence generation. More generally, every drag exerted on an air flow is associated to a loss of large scale kinetic energy and to an energy cascade from large scale kinetic energy to small scale turbulence (TKE) and ultimately to dissipation by molecular viscosity and conversion into enthalpy (Stull (1990), section 5.3).

In LMDZ, any drag parameterization “dg” calculates a wind tendency $[du/dt]_{dg}$, $[dv/dt]_{dg}$ for all vertical levels in each atmospheric column. This tendency can be expressed as the vertical divergence of a momentum stress $(\overline{\rho u w}_{dg}, \overline{\rho v w}_{dg})$, namely,

$$\left. \frac{\partial u}{\partial t} \right|_{\text{dg}} = -\frac{1}{\rho} \partial \frac{\overline{\rho \tilde{u} \tilde{w}}_{\text{dg}}}{\partial z}, \quad (\text{A1})$$

$$\left. \frac{\partial v}{\partial t} \right|_{\text{dg}} = -\frac{1}{\rho} \partial \frac{\overline{\rho \tilde{v} \tilde{w}}_{\text{dg}}}{\partial z}, \quad (\text{A2})$$

where ρ is the air density and u and v are the zonal and meridional components of the wind vector, respectively. The loss of kinetic energy k in an atmospheric layer associated to the parameterized drag “dg” thus reads

$$\left. \frac{\partial k}{\partial t} \right|_{\text{dg}} = -\delta z \left[u \frac{\partial \overline{\rho \tilde{u} \tilde{w}}_{\text{dg}}}{\partial z} + v \partial \frac{\overline{\rho \tilde{v} \tilde{w}}_{\text{dg}}}{\partial z} \right] = \delta z \underbrace{\left[\overline{\rho \tilde{u} \tilde{w}}_{\text{dg}} \frac{\partial u}{\partial z} + \overline{\rho \tilde{u} \tilde{w}}_{\text{dg}} \frac{\partial v}{\partial z} \right]}_{\Gamma_K(z)} - \delta z \underbrace{\left[\frac{\partial u \overline{\rho \tilde{u} \tilde{w}}_{\text{dg}}}{\partial z} + \frac{\partial v \overline{\rho \tilde{v} \tilde{w}}_{\text{dg}}}{\partial z} \right]}_{\Psi(z)}, \quad (\text{A3})$$

where δz is the depth of the considered atmospheric layer. We will see hereafter that Γ_K is an exchange term between large scale kinetic energy and TKE while Ψ corresponds to the vertical divergence of power associated to the parametrized stress. Once integrated over a whole atmospheric column, as $\int_0^\infty \Psi dz = 0$, Equation A3 reads

$$\partial_t K|_{\text{dg}} = \int_0^\infty \partial_z u \overline{\rho \tilde{u} \tilde{w}}_{\text{dg}} dz + \int_0^\infty \partial_z v \overline{\rho \tilde{v} \tilde{w}}_{\text{dg}} dz, \quad (\text{A4})$$

where

$$K = \int_0^\infty k dz = \int_0^\infty \rho \frac{(u^2 + v^2)}{2} dz \quad (\text{A5})$$

(Boville & Bretherton, 2003).

To guarantee energy conservation in LMDZ version 6A, $\partial_t K|_{\text{dg}}$ was initially calculated for each drag parameterization and then converted into enthalpy in each atmospheric column. To account for a more realistic mixing in the boundary-layer and to preclude artificial thermal decouplings over the continents, the loss of energy associated to the high-vegetation and orographic gravity-wave drag was then transferred to subgrid TKE before being converted into enthalpy, thereby enhancing the mixing in the boundary-layer. Practically, this is done as follows.

The parameterization of the vertical turbulent mixing in LMDZ version 6A is based on a local diffusion scheme combined with a mass-flux scheme for convective boundary layers, the so-called “thermal plume model” (Hourdin et al., 2002; Rio et al., 2010). The local diffusion scheme is a 1.5 order closure K-gradient scheme developed by Yamada (1983) in which the diffusion coefficients depend on the TKE calculated with a prognostic equation

$$\frac{\partial \text{TKE}}{\partial t} = \underbrace{\frac{1}{\rho} \frac{\partial}{\partial z} (\rho K_e \frac{\partial \text{TKE}}{\partial z})}_{\text{Turbulent diffusion}} - \underbrace{\overline{u'w'} \frac{\partial u}{\partial z} - \overline{v'w'} \frac{\partial v}{\partial z}}_{\text{Shear production}} + \underbrace{\frac{g}{\theta_v} \overline{w'\theta'_v}}_{\text{Buoyancy term}} - \underbrace{\frac{\text{TKE}^{3/2}}{cl}}_{\text{Dissipation}}, \quad (\text{A6})$$

where c is a real constant, θ_v the virtual potential temperature, $\overline{u'w'}$ and $\overline{v'w'}$ the components of the turbulent momentum flux, $\frac{g}{\theta_v} \overline{w'\theta'_v}$ the buoyancy flux, and K_e a turbulent diffusion coefficient.

The conversion of large scale energy into TKE due to the orographic gravity-wave drag and high-vegetation drag can therefore be taken into account by including the Γ_K terms associated to those parameterizations as additional “shear production” terms into Equation A6. For the vegetation, the drag coefficient is proportional to the fraction of protruding vegetation in the grid-box. More details and sensitivity tests can be found in Vignon (2017). One might also want to add the TKE tendency due to the flow-blocking component of the

subgrid orographic drag scheme. However, the underlying physical mechanism responsible for the energy cascade associated to flow blocking is not a priori obvious. This aspect deserves further investigation.

Appendix B: A Posteriori Correction of the Screen-Level Variables

B1 Diagnostics at the Screen Level

The calculation of the screen-level variables, tas (2 m temperature), $huss$ (2 m specific humidity), and uas and vas (eastward and northward surface wind) is done iteratively following Hess (1995). It is based on the Monin-Obukhov similarity theory for the surface layer and the bulk formulation of the turbulent flux proposed by Louis et al. (1982). The 2 m relative humidity, $hurs$, is then diagnosed from $huss$ and the saturated specific humidity at temperature tas .

The wind, the temperature, and the specific humidity profiles in the surface layer follow equations:

$$\begin{cases} \frac{\kappa u}{u_*} = \ln\left(\frac{z}{z_{0m}}\right) - \Psi_M\left(\frac{z}{L}\right) \\ \frac{(\Theta - \Theta_s)}{\Theta_*} = \frac{1}{\kappa} \left(\ln\left(\frac{z}{z_{0h}}\right) - \Psi_H\left(\frac{z}{L}\right) + \Psi_H\left(\frac{z_{oh}}{L}\right) \right) \\ \frac{(q - q_{surf})}{q_*} = \frac{1}{\kappa} \left(\ln\left(\frac{z}{z_{0h}}\right) - \Psi_H\left(\frac{z}{L}\right) + \Psi_H\left(\frac{z_{oh}}{L}\right) \right), \end{cases} \quad (B1)$$

with κ the empirical von Karman constant, L the Monin-Obukhov length, and Ψ the stability functions for the stability parameter $\zeta = \frac{z}{L}$. u_* is the friction velocity, Θ_* the temperature scale, and q_* the humidity

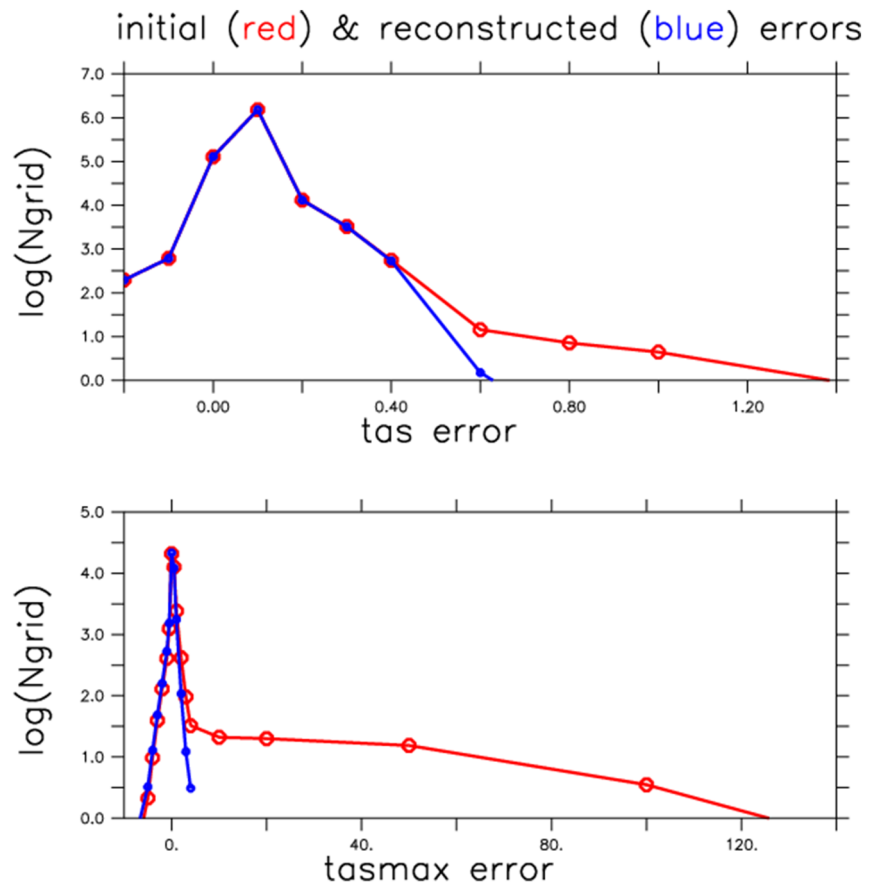


Figure B1. Cumulated histogram of the reconstruction errors for daily 2 m t . The y-axis is logarithmic. The red curve corresponds to the difference between the daily mean obtained with the original run and with the instantaneous values bounded with the surface and first atmospheric level temperature (ON experiment). The blue curve corresponds to the a posteriori correction.

scale. An empirical formulation for the stability functions is given by Dyer (1974). According to the Monin-Obukhov theory, L , u_* , Θ_* , and q_* are evaluated at the surface and are independent of z in the constant flux layer. A first guess of the screen variables is estimated owing to Equation B1. Then the Louis bulk formulation and the scale variables are used to calculate an updated value of the screen level variables. In situations where the turbulence is vanishing and the atmosphere above the surface is dry but the surface soil moisture is significantly above the residual value, a wrong diagnostic of q_{surf} in ORCHIDEE led to inconsistencies in the stability diagnostics between the first-guess evaluation and the use of the Louis formulation. In such conditions, the calculation can produce unrealistic (overestimated) values of tas up to 450 K together with negative values of relative humidity. Luckily, apart from a few exceptional events, this occurs only one time a day at most. Thanks to that it was possible to a posteriori correct the screen level values for simulations for which the minimum daily relative humidity was archived. In the vast majority of cases, these failures occur in stable conditions. In such conditions $\Psi_H = -\frac{5z}{L}$ and one shows easily that Θ is a monotonous function of z , which implies that Θ is comprised between Θ_s , the surface temperature, and Θ_1 , the temperature at the first atmospheric level of the model. A simulation where the screen level temperature is bounded at each timestep with the surface and the air temperature at the first atmospheric level will then be used to validate the a posteriori correction.

B2. A Posteriori Correction for the Screen-Level Variables

The a posteriori reconstruction algorithm is described hereafter. The general idea of the algorithm is to replace the erroneous values (daily maximum air temperature, tas_{max} or surface daily minimum relative humidity, $hurs_{min}$) by an interpolation between the previous and the following day without failure. The rarity of the failure of the screen variable calculation makes this approach feasible. The erroneous values (failure) are detected by looking for negative values of $hurs_{min}$.

- Step 1: We detect possible failure by identifying all the grid points and days (of index k) for which the estimated near-surface humidity is negative.
- Step 2: We correct the daily mean temperature by correcting the maximum in the daily mean using information from the last and next day without failure as follows. For the derivation, we denote by T the 2 m temperature, tas . The daily average value will be noted $\bar{T} = \sum_1^N T_i / N$, where N is the number of timesteps i within a day and the maximum T_{max} . We introduce the daily maximum anomaly $D = T_{max} - \bar{T}$. We apply the interpolation in time between the last (l) and next (n) day without failure to D , leading to the corrected value $D^* = (1 - a)D_l + aD_n$ with $a = (k - l) / (n - l)$. Then we compute the corrected daily averaged temperature as \bar{T}^* noticing that

$$\bar{T}^* - \bar{T} = (T_{max}^* - T_{max}) / N = (\bar{T}^* - \bar{T} + D^* - D) / N, \quad (B2)$$

so that

$$\bar{T}^* = \bar{T} + (D^* - D) / (N - 1). \quad (B3)$$

- Step 3: We correct the maximum temperature from the corrected daily mean temperature \bar{T}^* and interpolated daily anomaly D^* as

$$T_{max}^* = \bar{T}^* + D^*, \quad (B4)$$

which can be written as well using Equation B3 as

$$T_{max}^* = \bar{T} + (\bar{T}^* - \bar{T}) + D^* = \bar{T} + \frac{ND^* - D}{N - 1}. \quad (B5)$$

For the daily values of tas , this approach leads to replacing a potential error of about $\frac{1}{96} \times 150$ K (for a maximum error of 150 K on the instantaneous value of the temperature, 96 being the number of timesteps in one day for LMDZ version 6) by an uncertainty of at most $\frac{1}{96}$ of the daily maximum anomaly (that is about $\frac{10K}{96}$), that is, more than 10 times less. For tas_{max} the reconstruction procedure avoids creating extremes based on erroneous (and unrealistic) screen variable values.

A similar three-step approach is applied to correcting the relative humidity but taking as an information from the last and previous day without failure, the ratio $R = \frac{RH_{min}}{\overline{RH}}$, so that the procedure reads

- Step 1: Same as for T.
- Step 2: We apply the interpolation in time between the last (l) and next (n) day without failure to R , leading to the corrected value $R^* = (1 - a)R_l + aR_n$ with $a = (k - l)/(n - l)$. Then we compute the corrected daily averaged relative humidity as \overline{RH}^* noticing that

$$\overline{RH}^* - \overline{RH} = (RH_{min}^* - RH_{min})/N = \frac{R^*\overline{RH}^* - RH_{min}}{N}, \quad (B6)$$

and the corrected values are calculated with the following equations.

$$\overline{RH}^* = \frac{\left(\overline{RH} - \frac{RH_{min}}{N}\right)}{\left(1 - \frac{R^*}{N}\right)}. \quad (B7)$$

- Step 3: We correct the minimum relative humidity from the corrected daily mean relative humidity \overline{RH}^* and interpolated ratio R^* as

$$RH_{min}^* = R^* \overline{RH}^*. \quad (B8)$$

B3. Evaluation of the Uncertainty Relying on the A Posteriori Correction

The a posteriori reconstruction (hereafter called OFF) is evaluated against the results of the near-surface temperature diagnosed on-line in the model (hereafter called ON) and bounded at each timestep with the surface and the air temperature at the first atmospheric level. In the ON experiment the bounding is applied only for diagnostic purpose and does not affect the behaviour of the model.

For each grid point and each day of the 36 years of an AMIP experiment, the reconstruction error is evaluated with the difference between the OFF and the ON experiments.

Figure B1 shows the cumulated histogram of reconstruction errors with the a posteriori method and the ON bounding method for the daily mean and maximum daily temperature. For the majority of grid points and days, the OFF and ON methods give similar results. The reconstruction error lies within the range (-0.2 K, 0.4 K). These small differences between the two methods for daily values show that the near-surface temperature is not fundamentally modified by the OFF correction compared to what would be obtained with an on-line correction. The reconstruction errors for the monthly mean near-surface temperature would have been negligible compared to the daily errors, being 30 times smaller than daily errors.

Data Availability Statement

The version of LMDZ and ORCHIDEE used for the production of CMIP6 will be made available at the following address (<http://www.lmd.jussieu.fr/~lmdz/pub>). In the ORCHIDEE community, the model is referred as “Orchidee Trunk,” which is the official version developed at IPSL. The version used for the specific simulations runs for this paper is the “svn” release 3427 in the *LMDZ6/branches/IPSLCM6.0.15* and the “svn” release 5626 in the *tags/ORCHIDEE_2_0/ORCHIDEE_OL* branche. Simulations data used in the present paper will be made available with a DOI if the paper is accepted for publication.

References

- Adler, R., Huffman, G., Chang, A., Ferraro, R., Xie, P., Janowiak, B., et al. (2003). The Version 2 Global Precipitation Climatology Project (GPCP) monthly precipitation analysis (1979–Present). *Journal of Hydrometeorology*, 4, 1147–1167.
- Ait-Mesbah, S., Dufresne, J. L., Cheruy, F., & Hourdin, F. (2015). The role of thermal inertia in the representation of mean and diurnal range of surface temperature in semiarid and arid regions. *Geophysical Research Letters*, 42, 7572–7580. <https://doi.org/10.1002/2015GL065553>

Acknowledgments

This work was supported by the DEPHY2 project funded by the French national program LEFE/INSU. The CMIP6 project at IPSL used the HPC resources of TGCC under the allocations 2016-A0030107732, 2017-R0040110492, and 2018-R0040110492 (project gencmip6) provided by GENCI. One of the authors (Y. Zhao) benefited from the French state aid managed by the ANR under the “Investissements d’avenir” program with the reference ANR-11-IDEX-0004 - 17-EURE-0006. This study benefited from the ESPRI (Ensemble de Services Pour la Recherche l’IPSL) computing and data centre (<https://mesocentre.ipsl.fr>), which is supported by CNRS, Sorbonne Université, Ecole Polytechnique, and CNES and through national and international grants. Analysis presented in 4.14.1 benefited from the support of the CMUG and ESA-CCI programs (<http://www.esa-cmug-cci.org>). We also thank two anonymous reviewers for their helpful comments on the original manuscript.

- Al-Yaari, A., Ducharne, A., Cheruy, F., Crow, W. T., & Wigneron, J. P. (2019). Satellite-based soil moisture provides missing link between summertime precipitation and surface temperature biases in CMIP5 simulations over conterminous United States. *Scientific Reports*, 9, 1657. <https://doi.org/10.1038/s41598-018-38309-5>
- Arnell, N. W., & Gosling, S. N. (2013). The impacts of climate change on river flow regimes at the global scale. *Journal of Hydrology*, 486, 351–364. <https://doi.org/10.1016/j.jhydrol.2013.02.010>
- Betts, A. K., Ball, J. H., Beljaars, A. C. M., Miller, M. J., & Viterbo, P. A. (1996). The land surface-atmosphere interaction: A review based on observational and global modeling perspectives. *Journal of Geophysical Research*, 101(D3), 7209–7225. <https://doi.org/10.1029/95JD02135>
- Boé, J. (2013). Modulation of soil moisture/precipitation interactions over France by large scale circulation. *Climate Dynamics*, 40, 875–892. <https://doi.org/10.1007/s00382-012-1380-6>
- Boé, J., & Terray, L. (2008). Uncertainties in summer evapotranspiration changes over Europe and implications for regional climate change. *Geophysical Research Letters*, 35, L05702. <https://doi.org/10.1029/2007GL032417>
- Bontemps, S., Boettcher, M., Brockmann, C., Kirches, G., Lamarche, C., Radoux, J., et al. (2015). Multi-year global land cover mapping at 300 M and characterization for climate modelling: Achievements of the land cover component of the ESA climate change initiative. In *International Archives of the Photogrammetry, Remote Sensing and Spatial Information Sciences* (pp. 323–328). <https://doi.org/10.5194/isprsarchives-XL-7-W3-323-2015>
- Boone, A., & Etchevers, P. (2001). An intercomparison of three snow schemes of varying complexity coupled to the same land surface model: Local-scale evaluation at an Alpine site. *Journal of Hydrometeorology*, 2(4), 374–394. [https://doi.org/10.1175/1525-7541\(2001\)002<0374:AIOTSS>2.0.CO;2](https://doi.org/10.1175/1525-7541(2001)002<0374:AIOTSS>2.0.CO;2)
- Boucher, O., Servonnat, J., Albright, A. L., Aumont, O., Balkanski, Y., Bastrikov, V., et al. (2020). Presentation and evaluation of the IPSL-CM6A-LR climate model. *Journal of Advances in Modeling Earth Systems*, 12, e2019MS002010. <https://doi.org/10.1029/2019MS002010>
- Boville, B. A., & Bretherton, C. S. (2003). Heating and kinetic energy dissipation in the NCAR community atmosphere model. *Journal of Climate*, 16, 3877–3887. <https://doi.org/10.1175/1520-0442>
- Campoy, A., Ducharne, A., Cheruy, F., Hourdin, F., Polcher, J., & Dupont, J. C. (2013). Response of land surface fluxes and precipitation to different soil bottom hydrological conditions in a general circulation model. *Journal of Geophysical Research: Atmospheres*, 118, 10,725–10,739. <https://doi.org/10.1002/jgrd.50627>
- Chalita, S., & Le Treut, H. (1994). The albedo of temperate and boreal forest and the Northern Hemisphere climate: A sensitivity experiment using the LMD GCM. *Climate Dynamics*, 10, 231–240. <https://doi.org/10.1007/BF00208990>
- Cheruy, F., Campoy, A., Dupont, J. C., Ducharne, A., Hourdin, F., Haefelin, M., et al. (2013). Combined influence of atmospheric physics and soil hydrology on the simulated meteorology at the SIRTa atmospheric observatory. *Climate Dynamics*, 40, 2251–2269. <https://doi.org/10.1007/s00382-012-1469-y>
- Cheruy, F., Dufresne, J. L., Ait Mesbah, S., Grandpeix, J. Y., & Wang, F. (2017). Role of soil thermal inertia in surface temperature and soil moisture-temperature feedback. *Journal of Advances in Modeling Earth Systems*, 9, 2906–2919. <https://doi.org/10.1002/2017MS001036>
- Cheruy, F., Dufresne, J. L., Hourdin, F., & Ducharne, A. (2014). Role of clouds and land-atmosphere coupling in midlatitude continental summer warm biases and climate change amplification in CMIP5 simulations. *Geophysical Research Letters*, 41, 6493–6500. <https://doi.org/10.1002/2014GL061145>
- Coindreau, O., Hourdin, F., Haefelin, M., Mathieu, A., & Rio, C. (2007). Assessment of physical parametrizations using a global climate model with stretchable grid and nudging. *Monthly Weather Review*, 135, 1474–1490. <https://doi.org/10.1175/MWR3338.1>
- d'Orgeval, T., Polcher, J., & de Rosnay, P. (2008). Sensitivity of the West African hydrological cycle in ORCHIDEE to infiltration processes. *Hydrology and Earth System Sciences*, 12, 1387–1401.
- De Rosnay, P., Polcher, J., Bruen, M., & Laval, K. (2002). Impact of a physically based soil water flow and soil-plant interaction representation for modeling large-scale land surface processes. *Journal of Geophysical Research*, 107(D11), 4118. <https://doi.org/10.1029/2001JD000634>
- Dee, D., Uppala, S., Simmons, A., Berrisford, P., Poli, P., Kobayashi, S., et al. (2011). The ERA-Interim reanalysis: Configuration and performance of the data assimilation system. *Quarterly Journal of the Royal Meteorological Society*, 137(656), 553–597.
- Diallo, F. B., Hourdin, F., Rio, C., Traore, A. K., Mellul, L., Guichard, F., & Kergoat, L. (2017). The surface energy budget computed at the grid-scale of a climate model challenged by station data in West Africa. *Journal of Advances in Modeling Earth Systems*, 9, 2710–2738. <https://doi.org/10.1002/2017MS001081>
- Dorigo, W., Wagner, W., Albergel, C., Albrecht, F., Balsamo, G., Brocca, L., et al. (2017). ESA CCI Soil Moisture for improved Earth system understanding: State-of-the art and future directions. *Remote Sensing of Environment*.
- Ducoudré, N., Laval, K., & Perrier, A. (1993). SECHIBA, a new set of parametrizations of the hydrologic exchanges at the land-atmosphere interface within the LMD atmospheric general circulation model. *Journal of Climate*, 6, 248–273.
- Dyer, A. J. (1974). A review of flux-profile relationships. *Boundary-Layer Meteorology*, 7, 363–372. <https://doi.org/10.1007/BF00240838>
- Eltahir, E. A. B. (1998). A soil moisture rainfall feedback mechanism: 1. Theory and observations. *Water Resources Research*, 34(4), 765–776. <https://doi.org/10.1029/97WR03499>
- Eyring, V., Bony, S., Meehl, G. A., Senior, C. A., Stevens, B., Stouffer, R. J., & Taylor, K. E. (2016). Overview of the Coupled Model Intercomparison Project Phase 6 (CMIP6) experimental design and organization. *Geoscientific Model Development*, 9(5), 1937–1958. <https://doi.org/10.5194/gmd-9-1937-2016>
- Famiglietti, J. S. (2014). The global groundwater crisis. *Nature Climate Change*, 4(11), 945–948.
- Finnigan, J. (2000). Turbulence in plant canopies. *Annual Review of Fluid Mechanics*, 32(1), 519–571. <https://doi.org/10.1146/annurev.fluid.32.1.519>
- Garratt, J. R., & Hicks, B. B. (1973). Momentum, heat and water vapour transfer to and from natural and artificial surfaces. *Quarterly Journal of the Royal Meteorological Society*, 99(422), 680–687. <https://doi.org/10.1002/qj.49709942209>
- Gastineau, G., Lott, F., Mignot, J., & Hourdin, F. (2020). Alleviation of an arctic sea ice bias in a coupled model through modifications in the subgrid-scale orographic parameterization. *Journal of Advances in Modeling Earth Systems*, 12, e2020MS002111. <https://doi.org/10.1029/2020MS002111>
- Genthon, C., Six, D., Gallée, H., Grigioni, P., & Pellegrini, A. (2013). Two years of atmospheric boundary layer observations on a 45-m tower at Dome C on the Antarctic Plateau. *Journal of Geophysical Research: Atmospheres*, 118, 3218–3232. <https://doi.org/10.1002/jgrd.50128>
- Gouttevin, I., Krinner, G., Ciais, P., Polcher, J., & Legout, C. (2012). Multi-scale validation of a new soil freezing scheme for a land-surface model with physically-based hydrology. *The Cryosphere*, 6(2), 407–430. <https://doi.org/10.5194/tc-6-407-2012>
- Guilloid, B., Orlovsky, B., Miralles, D., Teuling, A. J., & Seneviratne, S. I. (2015). Reconciling spatial and temporal soil moisture effects on afternoon rainfall. *Nature Communication*, 6, 6443. <https://doi.org/10.1038/ncomms7443>

- Guimberteau, M., Drapeau, G., Ronchail, J., Sultan, B., Polcher, J., Martinez, J. M., et al. (2012). Discharge simulation in the sub-basins of the Amazon using ORCHIDEE forced by new datasets. *Hydrology and Earth System Sciences*, *16*(3), 911–935. <https://doi.org/10.5194/hess-16-911-2012>
- Guimberteau, M., Ducharne, A., Ciais, P., Boisier, J. P., Peng, S., De Weirdt, M., & Verbeeck, H. (2014). Testing conceptual and physically based soil hydrology schemes against observations for the Amazon Basin. *Geoscientific Model Development*, *7*(3), 1115–1136. <https://doi.org/10.5194/gmd-7-1115-2014>
- Guimberteau, M., Laval, K., Perrier, A., & Polcher, J. (2012). Global effect of irrigation and its impact on the onset of the Indian summer monsoon. *Climate Dynamics*, *39*, 1329. <https://doi.org/10.1007/s00382-011-1252-5>
- Guimberteau, M., Zhu, D., Maignan, F., Huang, Y., Yue, C., Dantec-Nédélec, S., et al. (2018). ORCHIDEE-MICT (v8. 4.1), a land surface model for the high latitudes: model description and validation. *Geoscientific Model Development*, *11*(1), 121–163. <https://doi.org/10.5194/gmd-11-121-2018>
- Haarsma, R. J., Roberts, M. J., Vidale, P. L., Senior, C. A., Bellucci, A., Bao, Q., et al. (2016). High Resolution Model Intercomparison Project (HighResMIP v1.0) for CMIP6. *Geoscientific Model Development*, *9*(11), 4185–4208. <https://doi.org/10.5194/gmd-9-4185-2016>
- Harris, I., Jones, P., Osborn, T., & Lister, D. (2014). Updated high-resolution grids of monthly climatic observations the CRU TS3.10 Dataset. *International Journal of Climatology*, *34*(3), 623–642. <https://doi.org/10.1002/joc.3711>
- Hess, R. (1995). On computing screen temperatures, humidities and anemometer-height winds in large-scale models. *Australian Meteorological Magazine*, *44*, 139–145.
- Hohenegger, C., Brockhaus, P., Bretherton, C., & Schär, C. (2009). The soil moisture precipitation feedback in simulations with explicit and parameterized convection. *Journal of Climate*, *22*(19), 5003–5020. <https://doi.org/10.1175/2009JCLI2604.1>
- Hohenegger, C., & Stevens, B. (2018). The role of the permanent wilting point in controlling the spatial distribution of precipitation. *Proceedings of the National Academy of Sciences*, *11*, 5692–5697. <https://doi.org/10.1073/pnas.1718842115>
- Holton, J. R. (2004). *An Introduction to Dynamic Meteorology*. Academic Press.
- Hourdin, F. (1992). Etude et simulation numérique de la circulation générale des atmosphères planétaires (in french) (PhD thesis). Paris, France: Laboratoire de Météorologie Dynamique.
- Hourdin, F., Couvreux, F., & Menut, L. (2002). Parameterization of the dry convective boundary layer based on a mass flux representation of thermals. *Journal of the Atmospheric Sciences*, *59*, 1105–1123.
- Hourdin, F., Grandpeix, J. Y., Rio, C., Bony, S., Jam, A., Cheruy, F., et al. (2013). LMDZ5B: The atmospheric component of the IPSL climate model with revisited parameterizations for clouds and convection. *Climate Dynamics*, *40*(9), 2193–2222. <https://doi.org/10.1007/s00382-012-1343-y>
- Hourdin, F., Jam, C., Rio, Couvreux, Sandu, I., Lefebvre, M. P., Brient, F., & Idelkadi, A. (2019). Unified parameterization of convective boundary layer transport and clouds with the thermal plume model. *Journal of Advances in Modeling Earth Systems*, *11*, 2910–2933. <https://doi.org/10.1029/2019MS001666>
- Hourdin, F., Mauritsen, T., Gettelman, A., Golaz, J. C., Balaji, V., Duan, Q., et al. (2017). The art and science of climate model tuning. *Bulletin of the American Meteorological Society*, *98*(3), 589–602. <https://doi.org/10.1175/BAMS-D-15-00135.1>
- Hourdin, F., Musat, I., Bony, S., Braconnot, P., Codron, F., Dufresne, J. L., et al. (2006). The LMDZ4 general circulation model: Climate performance and sensitivity to parametrized physics with emphasis on tropical convection. *Climate Dynamics*, *27*, 787–813. <https://doi.org/10.1007/s00382-006-0158-0>
- Hourdin, F., Rio, C., Grandpeix, J., Madeleine, J., Cheruy, F., Rochetin, N., et al. (2020). LMDZ6A: The atmospheric component of the IPSL climate model with improved and better tuned physics. *Journal of Advances in Modeling Earth Systems*, *12*, e2019MS001892. <https://doi.org/10.1029/2019MS001892>
- Hurt, G. C., Chini, L. P., Frolicking, S., Betts, R. A., Feddema, J., Fischer, G., et al. (2011). Harmonization of land-use scenarios for the period 1500–2100: 600 years of global gridded annual land-use transitions, wood harvest, and resulting secondary lands. *Climatic Change*, *109*(107). <https://doi.org/10.1007/s10584-011-0153-2>
- Jaeger, E., & Seneviratne, S. (2011). Impact of soil moisture atmosphere coupling on European climate extremes and trends in a regional climate model. *Climate Dynamics*, *36*, 1919–1939.
- Jakobson, E., Vihma, T., Palo, T., Jakobson, L., Keernik, H., & Jaagus, J. (2012). Validation of atmospheric reanalyses over the central Arctic Ocean. *Geophysical Research Letters*, *39*, L10802. <https://doi.org/10.1029/2012GL051591>
- Jung, M., Reichstein, M., Margolis, H. A., Cescatti, A., Richardson, A. D., Arain, M. A., et al. (2011). Global patterns of land-atmosphere fluxes of carbon dioxide, latent heat, and sensible heat derived from eddy covariance, satellite, and meteorological observations. *J. Geophys. Res.*, *116*, G00J07. <https://doi.org/10.1029/2010JG001566>
- Kato, S., Loeb, N. G., Rose, F. G., Doelling, D. R., Rutan, D. A., Caldwell, T. E., et al. (2013). Surface irradiances consistent with CERES-derived top-of-atmosphere shortwave and longwave irradiances. *Journal of Climate*, *26*, 2719–2740. <https://doi.org/10.1175/JCLI-D-12-00436.1>
- King, J. C., Connolley, W. M., & Derbyshire, S. H. (2001). Sensitivity of modelled Antarctic climate to surface and boundary layer flux parameterizations. *Quarterly Journal of the Royal Meteorological Society*, *127*(573), 779–794. <https://doi.org/10.1002/qj.49712757304>
- Klein, S. A., Jiang, X., Boyle, J., Malyshev, S., & Xie, S. (2006). Diagnosis of the summertime warm and dry bias over the U.S. Southern Great Plains in the GFDL climate model using a weather forecasting approach. *Geophysical Research Letters*, *33*, L18805. <https://doi.org/10.1029/2006GL027567>
- Koster, R., Dirmeyer, P., Guo, Z., Bonan, G., Chan, E., Cox, P., et al. (2004). Regions of strong coupling between soil moisture and precipitation. *Science*, *305*(5687), 1138.
- Koster, R. D., Guo, Z., Yang, R., Dirmeyer, P. A., Mitchell, K., & Puma, M. J. (2009). On the nature of soil moisture in land surface models. *Journal of Climate*, *22*(16), 4322–4335. <https://doi.org/10.1175/2009JCLI2832.1>
- Kottek, M., Grieser, J., Beck, C., Rudolf, B., & Rubel, F. (2006). World Map of the Köppen-Geiger climate classification updated. *Meteorologische Zeitschrift*, *15*, 259–263. <https://doi.org/10.1127/0941-2948/2006/0130>
- Krishnan, R., Sabin, T. P., Madhura, R. K., Vellore, R. K., Mujumdar, M., Sanjay, J., et al. (2019). Non-monsoonal precipitation response over the Western Himalayas to climate change. *Climate Dynamics*, *52*(7), 4091–4109. <https://doi.org/10.1007/s00382-018-4357-2>
- Laval, K. (1988). Experience with surface processes at LMD. *Workshop on Parametrization of Fluxes over Land Surface*. Shinfield Park, Reading: ECMWF. <https://www.ecmwf.int/node/10662>
- Le Quéré, C., Andrew, R. M., Friedlingstein, P., Sitch, S., Hauck, J., Pongratz, J., et al. (2018). Global carbon budget 2018. *Earth System Science Data*, *10*(4), 2141–2194.

- Li, S., Rupp, D. E., Hawkins, L., Mote, P. W., McNeill, D., Sparrow, S. N., et al. (2019). Reducing climate model biases by exploring parameter space with large ensembles of climate model simulations and statistical emulation. *Geoscientific Model Development*, *12*(7), 3017–3043. <https://doi.org/10.5194/gmd-12-3017-2019>
- Lindsay, R., Wensnahan, M., Schweiger, A., & Zhang, J. (2014). Evaluation of seven different atmospheric reanalysis products in the Arctic. *Journal of Climate*, *27*(7), 2588–2606. <https://doi.org/10.1175/JCLI-D-13-00014.1>
- Lott, F. (1998). Linear mountain drag and averaged pseudo-momentum flux profiles in the presence of trapped lee waves. *Tellus*, *50A*, 12–25.
- Lott, F. (1999). Alleviation of stationary biases in a GCM through a mountain drag parametrization scheme and a simple representation of mountain lift forces. *Monthly Weather Review*, *127*, 788–800.
- Lott, F., & Miller, M. J. (1997). A new subgrid-scale orographic drag parametrization: Its formulation and testing. *Quarterly Journal of the Royal Meteorological Society*, *123*, 101–127.
- Louis, J. F., Tiedtke, M., & Geleyn, J. F. (1982). A short history of the PBL parameterization at ECMWF, *Workshop on planetary boundary layer parameterization, 25-27 november 1981* (pp. 59–79). Shinfield Park, Reading: ECMWF.
- Lurton, T., Balkanski, Y., Bastrikov, V., Bekki, S., Bopp, L., Braconnot, P., et al. (2020). Implementation of the CMIP6 Forcing Data in the IPSL-CM6A-LR Model. *Journal of Advances in Modeling Earth Systems*, *12*, e2019MS001940. <https://doi.org/10.1029/2019MS001940>
- Malhi, Y. (1996). The behaviour of the roughness length for temperature over heterogeneous surfaces. *Quarterly Journal of the Royal Meteorological Society*, *533*, 1095–1125. <https://doi.org/10.1002/qj.49712253305>
- Manabe, S. (1969). Climate and the ocean circulation I. The atmospheric circulation and the hydrology of the Earth's surface. *Monthly Weather Review*, *97*(11), 739–774.
- Martens, B., Miralles, D. G., Lievens, H., van der Schalie, R., de Jeu, R. A. M., Fernández-Prieto, D., et al. (2017). GLEAM v3: satellite-based land evaporation and rootzone soil moisture. *Geoscientific Model Development*, *10*(5), 1903–1925. <https://doi.org/10.5194/gmd-10-1903-2017>
- Massman, W. (1999). A model study of kBH-1 for vegetated surfaces using "localized near-field" Lagrangian theory. *Journal of Hydrology*, *223*(1), 27–43. [https://doi.org/10.1016/S0022-1694\(99\)00104-3](https://doi.org/10.1016/S0022-1694(99)00104-3)
- Masson, V., & Seity, Y. (2009). Including atmospheric layers in vegetation and urban offline surface schemes. *Journal of Applied Meteorology and Climatology*, *48*(7), 1377–1397. <https://doi.org/10.1175/2009JAMC1866.1>
- Ménégoz, M., Krinner, G., Balkanski, Y., Boucher, O., Cozic, A., Lim, S., et al. (2014). Snow cover sensitivity to black carbon deposition in the Himalayas: From atmospheric and ice core measurements to regional climate simulations. *Atmospheric Chemistry and Physics*, *14*(8), 4237–4249. <https://doi.org/10.5194/acp-14-4237-2014>
- Milliman, J. D., & Farnsworth, K. L. (2011). *River discharge to the coastal ocean: A global synthesis*. Cambridge University Press. <https://doi.org/10.1017/CBO9780511781247>
- Miralles, D. G., Teuling, A. J., van Heerwaarden, C. C., & Vilá-Guerau de Arellano, J. (2014). Mega-heatwave temperatures due to combined soil desiccation and atmospheric heat accumulation. *Nature Geoscience*, *7*, 756–761. <https://doi.org/10.1038/ngeo2141>
- Mlawer, E. J., Taubman, S. J., Brown, P. D., Iacono, M. J., & Clough, S. A. (1997). Radiative transfer for inhomogeneous atmospheres: RRTM, a validated correlated-k model for the longwave. *Journal of Geophysical Research*, *102*(D14), 16,663–16,682. <https://doi.org/10.1029/97JD00237>
- Morcrette, J. J. (1991). Radiation and cloud radiative properties in the European Centre for Medium Range Weather Forecasts forecasting system. *Journal of Geophysical Research*, *96*(D5), 9121–9132. <https://doi.org/10.1029/89JD01597>
- Morcrette, C. J., Van Weverberg, K., Ma, H. Y., Ahlgrim, M., Bazile, E., Berg, L. K., et al. (2018). Introduction to CAUSES: Description of weather and climate models and their near-surface temperature errors in 5-day hindcasts near the Southern Great Plains. *Journal of Geophysical Research: Atmospheres*, *123*, 2655–2683. <https://doi.org/10.1002/2017JD027199>
- Naudts, K., Chen, Y., McGrath, M. J., Ryder, J., Valade, A., Otto, J., & Luyssaert, S. (2016). Europe's forest management did not mitigate climate warming. *Science*, *351*(6273), 597–600.
- Naudts, K., Ryder, J., McGrath, M., Otto, J., Chen, Y., Valade, A., et al. (2015). A vertically discretised canopy description for ORCHIDEE (SVN r2290) and the modifications to the energy, water and carbon fluxes. *Geoscientific Model Development*, *8*, 2035–2065.
- Nepf, H. M. (1999). Drag, turbulence, and diffusion in flow through emergent vegetation. *Water Resources Research*, *35*(2), 479–489. <https://doi.org/10.1029/1998WR900069>
- Peterson, B. J., Holmes, R. M., McClelland, J. W., Vörösmarty, C. J., Lammers, R. B., Shiklomanov, A. I., et al. (2002). Increasing river discharge to the Arctic Ocean. *Science*, *298*(5601), 2171–2173. <https://doi.org/10.1126/science.1077445>
- Polcher, J. (2003). Les processus de surface à l'échelle globale et leur interaction avec l'atmosphère (in french), Habilitation à diriger des recherches thesis, Université Pierre et Marie-Curie (Paris, France).
- Puma, M., & Cook, B. (2010). Effects of irrigation on global climate during the 20th century. *Journal of Geophysical Research*, *115*, D16120. <https://doi.org/10.1029/2010JD014122>
- Reeves Eyre, J. E. J., & Zeng, X. (2017). Evaluation of Greenland near surface air temperature datasets. *The Cryosphere*, *11*(4), 1591–1605. <https://doi.org/10.5194/tc-11-1591-2017>
- Rio, C., Hourdin, F., Couvreux, F., & Jam, A. (2010). Resolved versus parametrized boundary-layer plumes. Part II: continuous formulations of mixing rates for mass-flux schemes. *Boundary-Layer Meteorology*, *135*, 469–483. <https://doi.org/10.1007/s10546-010-9478>
- Rio, C., Hourdin, F., Grandpeix, J.-Y., & Lafore, J.-P. (2009). Shifting the diurnal cycle of parametrized deep convection over land. *Geophysical Research Letters*, *36*, L07809. <https://doi.org/10.1029/2008GL036779>
- Robinson, D. A., Estilow, T. W., & Program, N. C. (2012). NOAA Climate Data Record (CDR) of Northern Hemisphere (NH) Snow Cover Extent (SCE), Version 1, 2019-07-03T18:47:12Z. <https://doi.org/10.7289/V5N014G9>
- Rochetin, N., Couvreux, F., Grandpeix, J. Y., & Rio, C. (2014). Deep convection triggering by boundary layer thermals. Part I: LES analysis and stochastic triggering formulation. *Journal of the Atmospheric Sciences*, *71*(2), 496–514. <https://doi.org/10.1175/JAS-D-12-0336.1>
- Rochetin, N., Grandpeix, J. Y., Rio, C., & Couvreux, F. (2014). Deep Convection Triggering by Boundary Layer Thermals. Part II: Stochastic Triggering Parameterization for the LMDZ GCM. *Journal of the Atmospheric Sciences*, *71*(2), 515–538. <https://doi.org/10.1175/JAS-D-12-0337.1>
- Roehrig, R., Bouniol, D., Guichard, F., Hourdin, F., & Redelsperger, J. L. (2013). The present and future of the west african monsoon: A process-oriented assessment of CMIP5 simulations along the AMMA Transect. *Journal of Climate*, *26*(17), 6471–6505. <https://doi.org/10.1175/JCLI-D-12-00505.1>
- Sabin, T. P., Krishnan, R., Ghattas, J., Denvil, S., Dufresne, J. L., Hourdin, F., & Pascal, T. (2013). High resolution simulation of the South Asian monsoon using a variable resolution global climate model. *Climate Dynamics*, *41*(1), 173–194. <https://doi.org/10.1007/s00382-012-1658-8>

- Sandu, I., Beljaars, A., Bechtold, P., Mauritsen, T., & Balsamo, G. (2013). Why is it so difficult to represent stably stratified conditions in numerical weather prediction (NWP) models? *Journal of Advances in Modeling Earth Systems*, 5, 117–133. <https://doi.org/10.1002/jame.20013>
- Sandu, I., van Niekerk, A., Shepherd, T. G., Vosper, S. B., Zadra, A., Bacmeister, J., et al. (2019). Impacts of orography on large-scale atmospheric circulation. *Npj Climate and Atmospheric Science*, 2, 1–8. <https://doi.org/10.1038/s41612-019-0065-9>
- Schär, C., Lüthi, D., Beyerle, U., & Heise, E. (1999). The soil-precipitation feedback: A process study with a regional climate model. *Journal of Climate*, 12, 722–741.
- Schewe, J., Heinke, J., Gerten, D., Haddeland, I., Arnell, N. W., Clark, D. B., et al. (2014). Multimodel assessment of water scarcity under climate change. *Proceedings of the National Academy of Sciences*, 111(9), 3245–3250. <https://doi.org/10.1073/pnas.1222460110>
- Sellers, P. J., Mintz, Y., Sud, Y. C., & Dalcher, A. (1986). A simple biosphere model (SIB) for use within general circulation models. *Journal of the Atmospheric Sciences*, 43(6), 505–531. [https://doi.org/10.1175/1520-0469\(1986\)043<0505:ASBMFU>2.0.CO;2](https://doi.org/10.1175/1520-0469(1986)043<0505:ASBMFU>2.0.CO;2)
- Seneviratne, S. I., Corti, T., Davin, E. L., Hirschi, M., Jaeger, E. B., Lehner, I., et al. (2010). Investigating soil moisture climate interactions in a changing climate: A review. *Earth-Science Reviews*, 99(3–4), 125–161. <https://doi.org/10.1016/j.earscirev.2010.02.004>
- Seneviratne, S. I., Nicolls, N., Easterling, D., Goodess, C. M., Kanae, S., Kossin, J., et al. (2012). Changes in climate extremes and their impacts on the naturalphysical environment. In C. B. Field et al. (Eds.), *Managing the risks of extreme events and disasters to advance climate change adaptation, A Special Report of Working Groups I and II of the Intergovernmental Panel on Climate Change (IPCC)* (pp. 109–230). Cambridge, UK and New York, NY: Cambridge University Press.
- Steenveeld, G. J., Holtslag, A. A. M., Nappo, C. J., van de Wiel, B. J. H., & Mahrt, L. (2008). Exploring the possible role of small-scale terrain drag on stable boundary layers over land. *Journal of Applied Meteorology and Climatology*, 47(10), 2518–2530. <https://doi.org/10.1175/2008JAMC1816.1>
- Stouffer, R. J., Eyring, V., Meehl, G. A., Bony, S., Senior, C., Stevens, B., & Taylor, K. E. (2017). CMIP5 scientific gaps and recommendations for CMIP6. *Bulletin of the American Meteorological Society*, 98(1), 95–105. <https://doi.org/10.1175/BAMS-D-15-00013.1>
- Stull, R. B. (1990). *An Introduction to Boundary Layer Meteorology*. Kluwer, Boston.
- Su, Z., Schumge, T., Kustas, W. P., & Massman, W. J. (2001). An evaluation of two models for estimation of the roughness height for heat transfer between the land surface and the atmosphere. *Journal of Applied Meteorology*, 40(11), 1933–1951. [https://doi.org/10.1175/1520-0450\(2001\)040<1933:AEOTMF>2.0.CO;2](https://doi.org/10.1175/1520-0450(2001)040<1933:AEOTMF>2.0.CO;2)
- Taylor, C. M., de Jeu, R. A. M., Guichard, F., Harris, P. P., & Dorigo, W. A. (2012). Afternoon rain more likely over drier soils. *Nature*, 4, 423–426. <https://doi.org/10.1038/nature11377>
- Taylor, C. M., Gounou, A., Guichard, F., Harris, P. P., Ellis, R. J., Couvreur, F., & de Kauwe, M. (2011). Frequency of Sahelian storm initiation enhanced over mesoscale soil-moisture patterns. *Nature Geoscience*, 4, 430–433. <https://doi.org/10.1038/ngeo1173>
- Van Weverberg, K., Morcrette, C. J., Petch, J., Klein, S. A., Ma, H. Y., Zhang, C., et al. (2018). CAUSES: Attribution of surface radiation biases in NWP and climate models near the U.S. Southern Great Plains. *Journal of Geophysical Research: Atmospheres*, 123, 3612–3644. <https://doi.org/10.1002/2017JD027188>
- Vignon, E. (2017). The extreme atmospheric boundary layer over the Antarctic Plateau and its representation in climate models (PhD thesis). Grenoble, France: Université Grenoble-Alpes.
- Vignon, E., Hourdin, F., Genthon, C., Gallée, H., Bazile, E., Lefebvre, M. P., & Madeleine, J.-B. (2017). Antarctic boundary layer parametrization in a general circulation model: 1-D simulations facing summer observations at Dome C. *Journal of Geophysical Research: Atmospheres*, 122, 6818–6843. <https://doi.org/10.1002/2017JD026802>
- Vignon, E., Hourdin, F., Genthon, C., Gallée, H., Bazile, E., Lefebvre, M. P., et al. (2017). Parametrization of the boundary layer over the Antarctic Plateau in a general circulation model: 1D simulations against summertime observations at Dome C. *Journal of Geophysical Research: Atmospheres*, 122, 6818–6843. <https://doi.org/10.1002/2017JD026802>
- Vignon, E., Hourdin, F., Genthon, C., Van de Wiel, B. J. H., Gallée, H., Madeleine, J. B., & Beaumet, J. (2018). Modeling the dynamics of the atmospheric boundary layer over the antarctic plateau with a general circulation model. *Journal of Advances in Model Earth Systems*, 10, 98–125. <https://doi.org/10.1002/2017MS001184>
- Vignon, E., van de Wiel, B. J. H., van Hooijdonk, I. G. S., Genthon, C., van der Linden, S. J. A., van Hooft, J. A., et al. (2017). Stable boundary layer regimes at dome c, antarctica: Observation and analysis. *Quarterly Journal of the Royal Meteorological Society*, 143(704), 1241–1253. <https://doi.org/10.1002/qj.2998>
- Vonder Haar, T. H., Bytheway, J. L., & Forsythe, J. M. (2012). Weather and climate analyses using improved global water vapor observations. *Geophysical Research Letters*, 39, L15802. <https://doi.org/10.1029/2012GL052094>
- Vuichard, N., Messina, P., Luyssaert, S., Guenet, B., Zaehle, S., Ghattas, J., et al. (2019). Accounting for carbon and nitrogen interactions in the global terrestrial ecosystem model ORCHIDEE (trunk version, rev 4999): Multi-scale evaluation of gross primary production. *Geoscientific Model Development*, 12(11), 4751–4779.
- Wang, F., Cheruy, F., & Dufresne, J. L. (2016). The improvement of soil thermodynamics and its effects on land surface meteorology in the IPSL climate model. *Geoscientific Model Development*, 9(1), 363–381. <https://doi.org/10.5194/gmd-9-363-2016>
- Wang, F., Ducharne, A., Cheruy, F., Lo, M. H., & Grandpeix, J. Y. (2018). Impact of a shallow groundwater table on the global water cycle in the IPSL land-atmosphere coupled model. *Climate Dynamics*, 50, 3505–3522. <https://doi.org/10.1007/s00382-017-3820-9>
- Wang, T., Ottlé, C., Boone, A., Ciais, P., Brun, E., Morin, S., et al. (2013). Evaluation of an improved intermediate complexity snow scheme in the ORCHIDEE land surface model. *Journal of Geophysical Research: Atmospheres*, 118, 6064–6079. <https://doi.org/10.1002/jgrd.50395>
- Wei, N., Zhou, L., & Dai, Y. (2017). Evaluation of simulated climatological diurnal temperature range in CMIP5 models from the perspective of planetary boundary layer turbulent mixing. *Climate Dynamics*, 49, 1–22. <https://doi.org/10.1007/s00382-016-3323-0>
- Williams, C. J. R., Allan, R. P., & Kniveton, D. R. (2012). Diagnosing atmosphere-land feedbacks in CMIP5 climate models. *Environmental Research Letters*, 7(4), 044003. <https://doi.org/10.1088/1748-9326/7/4/044003>
- Xie, S., McCoy, R. B., Klein, S. A., Cederwall, R. T., Wiscombe, W. J., Clothiaux, E. E., et al. (2010). Clouds and more: ARM climate modeling best estimate data: A new data product for climate studies. *Bulletin of the American Meteorological Society*, 91, 13–20.
- Yamada, T. (1983). Simulations of nocturnal drainage flows by a q^2 Turbulence Closure Model. *Journal of the Atmospheric Sciences*, 40, 91–106.
- Zeng, Z., Piao, S., Li, L. Z., Zhou, L., Ciais, P., Wang, T., et al. (2017). Climate mitigation from vegetation biophysical feedbacks during the past three decades. *Nature Climate Change*, 7(6), 432–436.
- Zobler, L. (1986). *A World Soil File for Global Climate Modeling*: National Aeronautics and Space Administration, Goddard Space Flight Center, Institute for Space Studies.